Supporting Information to accompany:

Uncommon Synergy Between Adsorption and Diffusion of Hexane Isomer Mixtures in MFI Zeolite Induced by Configurational Entropy Effects

Tobias Titze[1)], Christian Chmelik[(1)], Jörg Kärger[(1)], Jasper M. van Baten[(2)], and Rajamani Krishna[(2)*]

[(1)] Abteilung Grenzflächenphysik, Universität Leipzig, Linnéstrasse 5, D-04103 Leipzig, Germany

[(2)] Van 't Hoff Institute for Molecular Sciences, University of Amsterdam, Science Park 904, 1098 XH Amsterdam, The Netherlands

[*] Corresponding authors:

Email: r.krishna@uva.nl

Table of Contents

1. Preamble

This Supporting Information accompanying the article *Uncommon Synergy between Adsorption and Diffusion of Hexane Isomer Mixtures in MFI zeolite induced by Configurational Entropy Effects* provides details of (a) Infra-Red Microscopy measurement set-up, (b) IRM measurement procedure for adsorption equilibrium and transient uptake within MFI crystals, (c) Configurational-Bias Monte Carlo (CBMC) simulation data and comparisons with IRM measurements of adsorption equilibrium for pure components and binary mixtures, (d) Maxwell-Stefan diffusion equations for describing transient uptake of mixtures, (e) Methodology for simulation of transient uptake of binary mixtures, (f) Comparisons of experimental IRM uptake transience with simulations for each of the four experimental Runs.

Additionally video animations of MD simulations for diffusion of nC4/iC4 and nC6/2MP mixtures have been provided as Supplemental Materials. These animations provide some "feel", albeit qualitative, for traffic junction effects.

2. Infra-Red Microscopy (IRM) Measurement set-up

Absorbance and Beer-Lambert Laws

IR microscopy is based on monitoring characteristic absorption bands of the molecules under study. They are attributed to specific vibrations of the molecule by which their electric dipole moment is changed. For substances adsorbed in transparent porous media, the loss of intensity B of the passing light is described by the *Beer-Lambert law*

$$A = \log(B_0 / B) = \alpha_m cd \qquad (1)$$

provided the conditions of negligible diffraction and not too high pressures are fulfilled. A, the quantity detected in the measurements, denotes the absorbance, α_m is the coefficient of molar extinction and d is

the thickness of the medium. The absorbance is defined as $A = 1/\log T$, the inverse logarithm of the transmission $T = B/B_0$. The crux of A is its proportionality to the concentration c of the guest species.

By using guest molecules with different characteristic vibrations, mixture diffusion can be studied. For molecules with similar IR bands, like n-hexane and 2-methylpentane, one species might be used in its fully deuterated form. The relevant chemical and transport properties remain unchanged upon such replacement.

The IR experimental set-up

The IR micro-imaging device used in this study consists of a spectrometer (*Bruker Vertex 80v*) attached to an IR microscope (*Bruker Hyperion 3000*). In principle, it operates as all Fourier-Transform IR machines.[1, 2] The light can be recorded by a conventional single-element detector (MCT, mercury cadmium telluride). Here, the area of interest can be adjusted by a rectangular aperture. In this way, the concentration averaged of the whole crystal can be measured.[3-6] At first, background and sample scans are recorded as interferograms from a polychromatic MIR source, having a Michelson-Interferometer in the optical path. By Fourier transformation, the intensity of the IR light is recorded as a function of the wavelength. Then, following equation (1), the absorption spectra are calculated from the background and sample scans. Due to the non-linear design of the reflection elements of the microscope the influence of stray light is completely eliminated. The optical bench allows to record IR spectra with a time resolution of up to 0.2 s at a spectral resolution of 16 cm^{-1}.

Vacuum system and IR cell

The setup consists of a cylindrical IR cell (effective window diameter 22 mm, path length about 5 mm) attached to a static vacuum system (stainless steel, ¼" Swagelok tubing and valves) with a dry turbo-molecular pump and an attached gas bottle with the sorbate (see Figure 1). The IR quartz glass windows of the optical cell ensure transparency in a broad IR range. With the attached pressure transducers the pressure can be measured in the range from 10^{-3} to 10^{4} mbar. The gas tanks of the

vacuum system ensure a constant gas phase pressure during ad- or desorption steps. Following the IR signal of the gas phase in the immediate surrounding of the nanoporous crystals it was confirmed that step changes are accomplished within a fraction of a second and that the final pressure remains constant at the desired values. Hence, there is no need for functions which account for time-lag effects introduced by finite flow rates. In a previous publication[7] we have already shown that "heat effects" (apparent external resistances of mass transfer created by the dissipation of heat during ad- or desorption) are negligible in our experiments with individual crystals. This is one important advantage in comparison to setups running with crystal batches or self-supporting wafers.

Just to reiterate two main differences to conventionally used systems: (i) We operate without a carrier gas or continuous gas flow, i.e. with a static vacuum system; (ii) Only one individual crystal is investigated, instead of a batch or a self-supporting wafer.[6]

3. Infra-Red Microscopy (IR) Experiments

Preparation

Prior to the measurement, a few selected, freshly calcined Silicalite-1 (MFI-type) crystals (see ref.[8] for synthesis details) were introduced into the IR cell and activated under vacuum at 673 K for at least 24 hours. Then, the cell was mounted on the motorised platform of the IR microscope (see close-up in Figure 1). All experiments were carried out at room temperature, i.e. at 298 K. The guest molecules under study were n-hexane (nC6) in its deuterated form and 2-methylpentane (2MP).

For the measurement only one individual crystal was selected. The size of the selected coffin shaped crystal was about 25 μm x 25 μm x 180 μm (see snapshot taken in the viewing mode in the upper right corner of Figure 1).

Adsorption, and Desorption

Uptake or release experiments were initialized by step-changes in the gas phase surrounding the crystals. The redistribution of the molecules of the two species in the mixture can be followed, since the

deuterated molecules can be easily distinguished from the non-deuterated species by the differences in the IR vibrations, e.g. the C–D vs. the C–H vibrations.

To follow the adsorption or desorption of the guest molecules into or out of the crystal, absorption spectra were recorded in the IR-transmission mode of the microscope with a temporal resolution between 0.3 – 1.5 s using the single element detector; see Figure 2a. The spectral resolution was set to 16 cm^{-1}. Following the Beer-Lambert law (Equation (1)), changes in guest concentration were determined by following changes in the area under characteristic IR bands (normally the C–H or C–D band, enclosed by a straight baseline; see Figure 2b. No baseline corrections were required. Plotting the time evolution of the normalized band intensity gives the integral "uptake curve" (see Figure 2c) which can be compared with the simulated uptakes as discussed in a later section.

Adsorption Isotherms

The adsorption isotherms were calculated from the spectra recorded at the end of the different ad- or desorption steps, i.e. when equilibrium was established. Usually, gas phase spectra were taken as a background scan to subtract the gas phase contribution from the signal of the adsorbed molecules. The measured isotherms are obtained in relative values and therefore calibrated by comparison with the Configurational-Bias Monte Carlo (CBMC) data as discussed in a later section.

Integral Uptake Curves

"Uptake curves", averaging the guest loading over the whole crystal, were recorded with the single-element detector. In the experiments the pressure steps were chosen in a way that the change in the corresponding guest concentration in the crystal is sufficiently small to consider the steps as "differential". For each adsorption step the uptake curves were calibrated by the corresponding IAST/RAST calculations of adsorption equilibrium. The modelling of the transient uptake curves to obtain the diffusivities is discussed in a later section of this Supplemental Material.

4. CBMC simulation methodology

Configurational-Bias Monte Carlo (CBMC) simulations were carried out to determine the adsorption equilibrium for pure components (nC4, iC4, nC6, 2MP) and binary mixtures (mC4/iC4, and nC6/2MP) in MFI zeolite at 298 K. The CBMC simulation methodology is described in published works.[9-13]

We present below a brief summary of the CBMC simulation methodology. The linear and branched alkanes are described with a united-atom model, in which CH_3, CH_2, and CH groups are considered as single interaction centres. When these pseudo-atoms belong to different molecules or to the same molecule but separated by more than three bonds, the interaction is given by a Lennard-Jones potential. The Lennard-Jones parameters are chosen to reproduce the vapour-liquid curve of the phase diagram as shown in Siepmann et al.[14]. For simulations with linear and branched alkanes with two or more C atoms, the beads in the chain are connected by harmonic bonding potentials. A harmonic cosine bending potential models the bond bending between three neighboring beads, a Ryckaert-Bellemans potential controls the torsion angle. Details for the alkane model can be found in Dubbeldam et al.[9, 10]

Following Kiselev and co-workers[15], we consider the MFI zeolite lattice to be rigid and we assume that interactions of an alkane with the zeolite are dominated by the dispersive forces between alkane pseudo atoms and the oxygen atoms of the zeolite. This is a very common approximation because the large oxygen atoms account for most of the potential energy and essentially shield the much smaller silicon atoms. The oxygen-adsorbate potential is an effective potential which implicitly includes the Si-contribution. These interactions are described by a Lennard Jones potential, which parameters are given by Dubbeldam et al. [9, 10] The Lennard-Jones potentials are shifted and cut at 12 Å.

The simulation box size was 2×2×4 unit cells for MFI; it was verified that the size of the simulation box was large enough to yield reliable data on adsorption isotherms. Periodic boundary conditions were employed.

Adsorption isotherms are conveniently computed using Monte Carlo simulations in the grand-canonical ensemble. In this ensemble the temperature and chemical potentials are imposed. The average number of adsorbed molecules per unit cell of the zeolite follows from the simulations. The

characteristics of these type of simulations is that during the calculations attempts are made to change the total number of particles by making attempts to insert molecule into or remove molecules from the zeolite. To make these types of moves possible for the long chain alkanes, we use the Configurational-Bias Monte Carlo (CBMC) technique.[12, 13] Instead of inserting a molecule at a random position, in a CBMC simulation, a molecule is grown atom by atom in such a way that the "empty spots" in the zeolite are found. This growing scheme gives a bias that is removed exactly by adjusting the acceptance rules.[12, 13]

These simulations were performed in cycles and in each cycle, an attempt to perform one of the following moves was made:

(1) displacement of a randomly selected chain. The maximum displacement was adjusted to an overall acceptance of 50%.

(2) rotation of a chain around its center of mass. The chain is chosen at random and the maximum rotation angle is selected to accept 50% of the moves.

(3) partly regrowing of a chain; a chain is selected at random and part of the molecule is regrown using the CBMC scheme. It is decided at random which part of the chain is regrown and with which segment the regrowing is started. For branched alkanes, the approach in Vlugt et al.[12]

(4) exchange with a reservoir; it is decided at random whether to add or to remove a molecule from the zeolite following the acceptance rules derived in Vlugt et al.[12]

(5) change of identity (only in the case of mixtures); one of the components is selected at random and an attempt is made to change its identity.[12] The acceptance rules for these trial moves can be found in Frenkel and Smit .[13]

Typically the number of MC cycles performed is 10^7. Of these, 15% are displacements, 15% rotations, 15% partial re-growths, 50% exchanges with the reservoir and the remaining 5% of the moves were attempts to change the identity of a molecule.

The crystallographic data of all-silica MFI are available on the zeolite atlas website of the International Zeolite Association (IZA).[16] The crystal framework density ρ = 1796 kg m^{-3}. The pore

volume V_p = 0.165 cm^3/g. The MFI structure consists of a set of two intersecting 10-ring channels of 5.4 Å × 5.5 Å and 5.4 Å × 5.6 Å size; see Figure 3.

5. Experimental validation of CBMC simulations of pure component adsorption isotherms in MFI by comparison with experimental data from the literature

To establish the validity of CBMC simulations we performed a comprehensive comparison of CBMC simulations of pure component isotherm for linear and branched alkanes with 1 – 7 C atoms in MFI with experimental data on pure component isotherms from the literature.

Figure 4 presents a comparison of CBMC simulations of pure component isotherms for CH_4 (= C1), C_2H_6 (= C3), and C_3H_8 (= C3), at a variety of temperatures with the experimental data of Sun et al.[17] The CBMC simulations are in excellent agreement with experimental isotherm data for the entire range of temperatures.

The CBMC simulation results are presented in terms of the bulk phase gas fugacities, f_i. When comparing with experimental data from literature sources that are reported in terms of pressures, p_i, we have been meticulous in calculating the fugacity coefficients using the Peng-Robinson equation of state to ensure that the comparisons are made on a consistent basis. In all cases discussed in this work, the corrections for the fugacity coefficients were negligibly small.

Figure 5 presents a comparison of CBMC simulations of pure component isotherms for nC_4H_{10} (= nC4) at a variety of temperatures and experimental data of Sun et al.[17] and Zhu et al.[18] The agreement between CBMC and experiments is seen to be remarkably good. The CBMC simulation data are fitted with the dual-Langmuir-Freundlich model

$$\Theta_i = \Theta_{i,A,sat} \frac{b_{i,A} f_i^{\nu_A}}{1 + b_{i,A} f_i^{\nu_A}} + \Theta_{i,B,sat} \frac{b_{i,B} f_i^{\nu_B}}{1 + b_{i,B} f_i^{\nu_B}} \qquad (2)$$

with parameters specified in Table 1.

The loadings Θ_i are expressed in molecules per unit cell of MFI. The loadings q_i are expressed as mol per kg of MFI framework. The discussions of configurational entropy effects are much more convenient in terms of Θ_i. The loadings in terms of Θ_i need to be multiplied by a factor 0.1734 in order to obtain the molar loading q_i. The CBMC simulation results are presented in terms of the bulk phase gas fugacities, f_i. We have verified that the corrections for the fugacity coefficients are negligibly small for the conditions of the experiment reported in this paper.

Figure 6 presents a comparison of experimental isotherm data of Song and Rees [19] and Millot et al.[20, 21] for nC6 with CBMC simulations; good agreement is again observed for a variety of temperatures. The agreement between CBMC and experiments is good for all the temperatures. The nC6 isotherms exhibit a slight inflection in the adsorption isotherm at a loading Θ_i =4 molecules per unit cell, corresponding to 0.6935 mol kg^{-1} and the reasons for this are explained by Vlugt et al.[12]

The length of an n-heptane (nC7) molecule is slightly longer than the distance between adjacent intersections; see snapshot in Figure 7. The incommensurateness of the molecular length of nC7 with the periodicity of MFI causes the adsorption isotherms to exhibit an inflection at a loading Θ_i =4/uc; see Figure 7. The inflection characteristics, captured in CBMC simulations, are in accord with the experimental data of Sun et al.[22] and Eder.[23]

Figure 8 presents a comparison of CBMC simulations of pure component isotherms for iC_4H_{10} (= iC4) at a variety of temperatures compared with the experimental data of Sun et al.[17] and Zhu et al.[18] For all temperatures, the adsorption isotherms for iC4 exhibit strong inflection characteristic due to the fact that iC4 locates preferentially at the intersections between straight and zig-zag channels; these intersection sites offer more "leg room". There are 4 intersections per unit cell of MFI, and consequently the inflection is observed at a loading Θ_i = 4/uc, corresponding to q_i =0.6935 mol kg^{-1}. To obtain loadings higher than Θ_i =4/uc, an extra push is required to make the mono-branched locate within the channel interiors; this extra push is the cause of the inflection in the isotherm. The snapshot of adsorbed iC4 molecules at a loading Θ_i =4/uc demonstrates that only the intersections are occupied. The CBMC

simulations for iC4 at 298 K are fitted with the dual-Langmuir-Freundlich parameters specified in Table 1.

Figure 9 compares experimental isotherm data of Zhu et al.[24] for 2-methylpentane (= 2MP) with the corresponding CBMC simulations. The strong inflection in the CBMC data at a loading of 4 molecules per unit cell is evident. Vlugt et al.[12, 25] were the first to use CBMC simulations to provide a fundamental interpretation isotherm inflection characteristics for 2MP in terms of configurational effects and preferential location at the intersections of MFI zeolite.

A similar good agreement of CBMC simulations of the isotherm for 3MP with experimental data[24, 26] is obtained for 3-methylpentane (= 3MP); see Figure 10 .

The di-branched isomers 2,2 dimethylbutane (= 22DMB) and 2,3 dimethylbutane (23DMB) are too bulky to locate within the channels, and therefore only the intersection sites can be occupied, yielding a saturation loading $\Theta_{i,sat}$ =4/uc ($q_{i,sat}$ =0.6935 mol kg^{-1}); see Figure 11.

6. Calibration of IRM data on pure component isotherms

To obtain IRM data on pure component adsorption isotherms, the IR signal is measured at different gas phase pressures after sorption equilibrium is reached. The measured IR isotherm is obtained in units proportional to the concentration, not in the absolute concentration itself. To convert the relative concentration in absolute concentration, the IR signal needs to be calibrated. The calibration might be done in several ways, e.g. by comparing the signal with that of a sample loaded at a known guest concentration or by comparing the IR isotherm with other isotherms from literature or of the same sample batch but recorded using another device (e.g. gravimetric uptake).

In our case we followed the latter option. It is essential to note, that "comparing" refers to a rescaling of the entire isotherm (i.e. multiplying all values with one and the same factor) rather than rescaling each value itself differently. Certain characteristic points may ease the comparison, e.g. inflections or the saturation loading. In the current work, the nC6 and 2MP single component IR isotherms were calibrated on the basis of the CBMC simulations. Since the CBMC simulations have been

demonstrated to be in excellent agreement with published experimental data, the calibration of IRM pure component isotherm data with CBMC simulations is considered to be an acceptable procedure.

Figure 12 compares the CBMC simulations for nC6 with the calibarated IRM data. The CBMC data are fitted with the dual-Langmuir-Freundlich parameters specified in Table 2. Also shown in Figure 12 are snapshots showing the location of nC6 molecules within the straight and zig-zag channels of MFI. The length of the nC6 molecule is commensurate with the distance between intersections along the zig-zag channels and a maximum of 8 molecules in a unit cell can be accommodated in the straight and zig-zag channels.[12]

Figure 13 compares CBMC simulations of pure component isotherm for 2-methylpentane (= 2MP) with the corresponding calibrated IRM isotherm data. The CBMC simulations for 2MP at 298 K are fitted with the dual-Langmuir-Freundlich parameters specified in Table 2. Also shown is snapshot of 2MP molecules, again clearly indicating location at the intersection sites of MFI.

Once the calibration of the nC6 and 2MP single component IR isotherms were fixed these were used to determine the loadings in the mixture adsorption experiments and the transient uptake IRM data. It is to be noted that no further calibration was used.

7. Comparison of IRM data with CBMC simulations of mixture adsorption equilibrium

The stark differences in the pure component adsorption behaviors of linear and branched alkanes, can be exploited to separate mixtures containing linear from branched alkanes with the same number of carbon atoms. To illustrate this separation principle, let us consider CBMC simulations of loadings in the adsorbed phase in equilibrium with equimolar binary gas phase containing a mixture of nC6 and 2MP with equal partial pressures $p_1 = p_2$ in the bulk gas phase; see Figure 14a. Up to total hydrocarbons pressures $p_t = p_1 + p_2 = 2$ Pa, the component loadings Θ_i of each component increases in an expected manner; increasing p_t leads to a corresponding increase in the component loading Θ_i. At 2 Pa pressure the total loading $\Theta_t = 4$/uc, signifying that all the intersection sites are fully occupied. To further adsorb 2MP we need to provide an extra "push". Energetically, it is more efficient to obtain higher mixture

loadings by "replacing" the 2MP with nC6; this *configurational entropy* effect is the reason behind the curious maxima in the 2MP loading in the mixture.

The experimentally determined loadings from IRM are also plotted in Figure 14a. There is good agreement of the IRM data and the CBMC mixture simulations. The IRM experiments offer the first direct experimental verification of the configurational entropy effects in mixture adsorption for nC6/2MP that was first observed on the basis of CBMC mixture simulations.[12, 27] Figure 14b is a plot of the component loadings in the adsorbed mixture, Θ_I, as a function of the total mixture loading Θ_t. It is clear to see that configurational entropy effects manifest for loadings $\Theta_t > 4$/uc.[12, 27]

The influence of configurational entropy effects on separations is best quantified by the *adsorption selectivity* S_{ads}, defined by

$$S_{ads} = \frac{\Theta_1/\Theta_2}{p_1/p_2} = \frac{\Theta_1/\Theta_2}{f_1/f_2} \qquad (3)$$

For equimolar binary gas phase mixtures, Equation (3) simplifies to yield

$$S_{ads} = \frac{\Theta_1}{\Theta_2} \quad \text{(for equimolar gas mixture with } p_1 = p_2\text{)} \qquad (4)$$

The calculations of S_{ads} are shown in Figure 14c. We note that for total loadings $\Theta_t < 4$/uc, $S_{ads} \approx 1$, suggesting that adsorptive separations are not feasible in the pressures below $p_1 + p_2 < 2$ Pa. However, when the total loadings of the adsorbed phase Θ_t exceeds 4/uc, the values of S_{ads} increase significantly to values by about one to two orders of magnitude. This implies that sharp separations of the linear and branched hexanes are possible provided the operating conditions correspond to total mixture loadings $\Theta_t > 4$/uc.

Figure 15a presents IRM experimental data, obtained at 298 K, of loadings in the adsorbed phase in equilibrium with binary nC4/iC4 mixture with partial pressures $p_1 = p_2$ in the bulk gas phase; these data are in excellent agreement with the corresponding CBMC simulations. For nC4/iC4 mixture configurational entropy effects also cause the preferential adsorption of the linear nC4 molecule, but in this case the adsorption selectivities are not as high as those encountered earlier for nC6/2MP and

nC6/22DMB mixtures; see Figure 15b. The branched isomer iC4 is less strongly constrained within the channels of MFI than 2MP.

8. Modeling mixture adsorption equilibrium using IAST and RAST

We now examine how accurately configurational entropy effects in mixture adsorption are captured by calculations following the Ideal Adsorbed Solution Theory (IAST) of Myers and Prausnitz[28] using dual-Langmuir-Freundlich fits of the pure component isotherms. Briefly, the basic equation of IAST theory is the analogue of Raoult's law for vapour-liquid equilibrium, i.e.

$$p_t y_i = P_i^0(\Phi) x_i; \quad i = 1,2,...n \tag{5}$$

where x_i is the mole fraction in the adsorbed phase

$$x_i = \frac{q_i}{q_1 + q_2 + ...q_n} \tag{6}$$

and $P_i^0(\Phi)$ is the pressure for sorption of every component *i*, which yields the same surface potential, Φ_i^0 for each of the pure components, as that for the mixture, Φ:

$$\frac{\Phi}{RT} = \rho \int_{f=0}^{f=P_1^0} \frac{q_1^0(f)}{f} df = \rho \int_{f=0}^{f=P_1^0} \frac{q_2^0(f)}{f} df = \rho \int_{f=0}^{f=P_2^0} \frac{q_2^0(f)}{f} df = \rho \int_{f=0}^{f=P_3^0} \frac{q_3^0(f)}{f} df = ... \tag{7}$$

where *R* is the gas constant, ρ is the framework density of MFI and $q_i^0(f)$ is the *pure* component adsorption isotherm given by eq. (2). The total amount adsorbed is calculated from

$$q_t \equiv q_1 + q_2 ... + q_n = \frac{1}{\frac{x_1}{q_1(P_1^0)} + \frac{x_2}{q_2(P_2^0)} + ... + \frac{x_n}{q_n(P_n^0)}} \tag{8}$$

The set of equations eq. (2), (5), (6), (7) and (8) need to be solved numerically to obtain the loadings, q_i, (or equivalently Θ_i) of the individual components in the mixture.

Figure 16 compares the IAST calculations with CBMC simulations of component loadings of binary nC4/iC4, and nC6/2MP mixtures. For both mixtures, the IAST estimations of the component loadings

are of excellent accuracy for total mixture loadings Θ_t < 4/uc. For modeling the uptake of nC6/2MP mixtures within MFI crystals exposed to bulk gas pressures lower than 2 Pa (Runs 1 and 2), we use IAST in the model calculations presented in the Manuscript.

While the correct qualitative trends are prediction for Θ_t > 4/uc, the IAST estimations are not sufficiently accurate. The reasons for these deviations can be traced to the fact that the manifestation of configurational entropy effects at Θ_t < 4/uc implies strong segregation in the location of adsorbed molecules: branched molecules occupying only the intersections, while the linear molecules are located everywhere. A key assumption made in the derivation of the IAST is that there is a homogeneous distribution of the components in the adsorbed phase; this assumption is clearly violated for mixture adsorption of linear and branched alkanes in MFI. A detailed analysis, and quantification, of segregation effects for nC4/iC4 mixtures has been provided by Krishna and Paschek.[29]

A simple, pragmatic, approach to account for non-ideality effects in mixture adsorption is to introduce activity coefficients into eq. (5). The resulting Real Adsorbed Solution Theory (RAST) is described by

$$Py_i = P_i^0(\Phi) x_i \gamma_i \tag{9}$$

Following the work of Calleja et al.[30] we have used the Wilson model for the activity coefficients:

$$\begin{aligned} \ln(\gamma_1) &= 1 - \ln(x_1 + x_2\Lambda_{12}) - \frac{x_1}{x_1 + x_2\Lambda_{12}} - \frac{x_2\Lambda_{21}}{x_2 + x_1\Lambda_{21}} \\ \ln(\gamma_2) &= 1 - \ln(x_2 + x_1\Lambda_{21}) - \frac{x_2}{x_2 + x_1\Lambda_{21}} - \frac{x_1\Lambda_{12}}{x_1 + x_2\Lambda_{12}} \end{aligned} \tag{10}$$

The choice of $\Lambda_{12} = \Lambda_{21} = 1$ in Equation (10) reduces equation (9) to equation (5). The parameters Λ_{12} and Λ_{21} can be fitted to match the CBMC mixture simulations. Table 3 lists the Wilson non-ideality parameters Λ_{12} and Λ_{21} obtained in this manner for C4/iC4 and nC6/2MP mixtures. Figure 17 compares the RAST estimations with CBMC simulations of component loadings of the two binary mixtures. We observe a reasonably good agreement between CBMC simulation data and RAST calculations.

For modeling the uptake of nC6/2MP mixtures within MFI crystals exposed to bulk gas pressures exceeding 2 Pa (Runs 3 and 4), we use RAST in the model calculations presented in this article.

9. Maxwell-Stefan equations for mixture diffusion

The Maxwell-Stefan (M-S) equations for *n*-component diffusion inside porous crystalline materials can be written as

$$-\rho \frac{q_i}{RT}\nabla \mu_i = \sum_{\substack{j=1 \\ j\neq i}}^{n} \frac{x_j N_i - x_i N_j}{Đ_{ij}} + \frac{N_i}{Đ_i}; \quad i = 1,2,..n \tag{11}$$

For detailed derivations of Equation (11), the reader is referred to earlier publications.[31-33] In equation (11) the $Đ_i$ is the M-S diffusivities of species *i*, portraying the interaction between component *i* in the mixture with the surface, or wall of the structure. The fluxes N_i defined in equation (11) are expressed in terms of the number of moles of species *i* transported per m^2 of *crystalline material* per second. The $Đ_{ij}$ are M-S exchange coefficients representing interaction between component *i* with component *j*. At the molecular level, the $Đ_{ij}$ reflect how the facility for transport of species *i correlates* with that of species *j*. The x_i in equations (11) and represent the component mole fractions in the adsorbed phase within the pores and calculated from equation (6).

The Onsager reciprocal relations require

$$Đ_{ij} = Đ_{ji} \tag{12}$$

By defining an *n*-dimensional square matrix [*B*] with elements

$$B_{ii} = \frac{1}{Đ_i} + \sum_{\substack{j=1 \\ j\neq i}}^{n} \frac{x_j}{Đ_{ij}}; \qquad B_{ij} = -\frac{x_i}{Đ_{ij}}; \quad i, j = 1,2....n \tag{13}$$

we can recast equation (11) into the following form

$$-\rho \frac{q_i}{RT}\nabla \mu_i = \sum_{j=1}^{n} B_{ij} N_j; \quad i = 1,2,..n \tag{14}$$

The chemical potential gradients $\nabla \mu_i$ can be related to the gradients of the molar loadings, q_i, by defining thermodynamic correction factors Γ_{ij}

$$\frac{q_i}{RT}\nabla\mu_i = \sum_{j=1}^{n}\Gamma_{ij}\nabla q_j; \quad \Gamma_{ij} = \frac{q_i}{f_i}\frac{\partial f_i}{\partial q_j}; \quad i,j = 1,....n \tag{15}$$

In the special case in which each of the pure component adsorption isotherms is described by a single-site Langmuir model and a mixed gas Langmuir model is used to describe the mixture adsorption equilibrium we can derive the simple analytic expression[34]

$$\Gamma_{ij} = \delta_{ij} + \left(\frac{q_{i,sat}}{q_{j,sat}}\right)\left(\frac{\theta_i}{1-\theta_1-\theta_2-....-\theta_n}\right); \quad i,j = 1,2\ldots n \tag{16}$$

where the fractional occupancies, θ_i, are defined by

$$\theta_i \equiv \Theta_i / \Theta_{i,sat} = q_i / q_{i,sat} \tag{17}$$

Using the IAST or RAST calculations for the loadings Θ_1, Θ_2 in Equations (16) and (17) is an reasonably good approximation for calculating the elements of $\begin{bmatrix}\Gamma_{11} & \Gamma_{12}\\ \Gamma_{21} & \Gamma_{21}\end{bmatrix}$. The off-diagonal elements of the matrix $\begin{bmatrix}\Gamma_{11} & \Gamma_{12}\\ \Gamma_{21} & \Gamma_{21}\end{bmatrix}$ can have magnitudes significantly larger than unity. As illustration, Figure 18a presents the elements Γ_{ij} of the thermodynamic corrector factor matrix [Γ], obtained by differentiation of the IAST equations describing the nC6/2MP adsorption equilibrium. We note that for f_t < 1 Pa, the off-diagonal elements are significantly smaller in magnitude than the corresponding diagonal elements. However, for f_t > 1 Pa, the contribution of the off-diagonal elements becomes increasingly significant. Figure 18b presents calculations of ($\Gamma_{12}\,\Theta_2/\Gamma_{11}\,\Theta_1$) that signify the extent of thermodynamic coupling. We note that the driving force of 2MP is significantly influenced by that of nC6. Another interesting point to note is that ($\Gamma_{12}\,\Theta_2/\Gamma_{11}\,\Theta_1$) exhibits a maximum at a pressure of 2 Pa. Figure 18c presents calculations of ($\Gamma_{12}\,\Theta_2/\Gamma_{11}\,\Theta_1$) as a function of the total mixture loading, Θ_t. We note that the maximum in the value of ($\Gamma_{12}\,\Theta_2/\Gamma_{11}\,\Theta_1$) occurs at $\Theta_t \approx 4$ molecules/uc. We will see in a later section that this maximum leaves its strong imprint on the uptake kinetics in Run 1 of the IRM experiments.

The elements of the matrix of thermodynamic correction factors Γ_{ij} are more precisely determined by numerical differentiation of the equations describing mixture adsorption equilibrium, using either IAST or RAST; this requires robust numerical procedures.

For unary diffusion of component *i*, the Maxwell-Stefan relations simplify to yield

$$N_i = -\rho D_i \nabla q_i = -\rho Đ_i \Gamma_i \nabla q_i; \quad \Gamma_i = \frac{q_i}{f_i}\frac{\partial f_i}{\partial q_i}; \quad \text{unary system} \tag{18}$$

where the commonly used Fick diffusivity of species I is related to the unary Maxwell-Stefan diffusivity

$$D_i = Đ_i \Gamma_i; \quad \text{unary system} \tag{19}$$

Equation (14) can be re-written in *n*-dimensional matrix notation as

$$(N) = -\rho[B]^{-1}\,[\Gamma]\nabla(q) \tag{20}$$

Let us denote the inverse of [*B*] as [Δ]:

$$[B]^{-1} \equiv [\Delta] \tag{21}$$

For the special case of a binary mixture (*n* = 2) we obtain the explicit expression

$$[\Delta] \equiv [B]^{-1} = \begin{bmatrix} \dfrac{1}{Đ_1} + \dfrac{x_2}{Đ_{12}} & -\dfrac{x_1}{Đ_{12}} \\ -\dfrac{x_2}{Đ_{12}} & \dfrac{1}{Đ_2} + \dfrac{x_1}{Đ_{12}} \end{bmatrix}^{-1} \tag{22}$$

The matrix inversion can be carried out explicitly to yield the following expressions

$$\Delta_{11} = Đ_1 \frac{\left(1 + \dfrac{x_1 Đ_2}{Đ_{12}}\right)}{1 + \dfrac{x_1 Đ_2}{Đ_{12}} + \dfrac{x_2 Đ_1}{Đ_{12}}} \tag{23}$$

$$\Delta_{22} = Đ_2 \frac{\left(1+\frac{x_2 Đ_1}{Đ_{12}}\right)}{1+\frac{x_1 Đ_2}{Đ_{12}}+\frac{x_2 Đ_1}{Đ_{12}}} \tag{24}$$

$$\Delta_{12} = Đ_1 \frac{\frac{x_1 Đ_2}{Đ_{12}}}{1+\frac{x_1 Đ_2}{Đ_{12}}+\frac{x_2 Đ_1}{Đ_{12}}} \tag{25}$$

$$\Delta_{21} = Đ_2 \frac{\frac{x_2 Đ_1}{Đ_{12}}}{1+\frac{x_1 Đ_2}{Đ_{12}}+\frac{x_2 Đ_1}{Đ_{12}}} = \frac{x_2}{x_1}\Delta_{12} \tag{26}$$

In the limiting case of $x_1 \to 1; \quad x_2 \to 0$ we obtain

$$\Delta_{11} = \frac{Đ_1\left(1+\frac{x_1 Đ_2}{Đ_{12}}\right)}{1+\frac{x_1 Đ_2 + x_2 Đ_1}{Đ_{12}}} \to Đ_1; \quad x_1 \to 1; \quad x_2 \to 0 \tag{27}$$

In the limiting case of $x_2 \to 1; \quad x_1 \to 0$ we obtain

$$\Delta_{22} = \frac{Đ_2\left(1+\frac{x_2 Đ_1}{Đ_{12}}\right)}{1+\frac{x_2 Đ_1 + x_1 Đ_2}{Đ_{12}}} \to Đ_2; \quad x_2 \to 1; \quad x_1 \to 0 \tag{28}$$

For uptake of a binary mixture within a spherical crystal, the flux expressions for *r*-coordinate radial diffusion of a binary nC6/2MP mixture are summarized in matrix notation as follows

$$\begin{pmatrix} N_1 \\ N_2 \end{pmatrix} = -\rho \begin{bmatrix} \Delta_{11} & \Delta_{12} \\ \Delta_{21} & \Delta_{21} \end{bmatrix} \begin{bmatrix} \Gamma_{11} & \Gamma_{12} \\ \Gamma_{21} & \Gamma_{21} \end{bmatrix} \frac{\partial \begin{pmatrix} q_1 \\ q_2 \end{pmatrix}}{\partial r} \tag{29}$$

The flux of each species is strongly coupled to its partner in the mixture due to two types of couplings: (a) correlation effects that contribute to finite contributions of non-diagonal elements in

$\begin{bmatrix} \Delta_{11} & \Delta_{12} \\ \Delta_{21} & \Delta_{21} \end{bmatrix}$, and (b) thermodynamic coupling due to the non-diagonal elements of $\begin{bmatrix} \Gamma_{11} & \Gamma_{12} \\ \Gamma_{21} & \Gamma_{21} \end{bmatrix}$. The importance of the latter has already been demonstrated in the calculations presented in Figure 18. Let us now investigate the structure of $\begin{bmatrix} \Delta_{11} & \Delta_{12} \\ \Delta_{21} & \Delta_{21} \end{bmatrix}$ in more detail.

10. Intersection blocking and correlation effects

From equations (23), (24), (25) and (26) we see that there are three independent parameters that determine $\begin{bmatrix} \Delta_{11} & \Delta_{12} \\ \Delta_{21} & \Delta_{21} \end{bmatrix}$; these are $Đ_1$, $Đ_2$, and $(Đ_1/Đ_{12})$. On the basis of literature data, we now try to gain insights into these three parameters.

Schuring et al.[35] have reported experimental data on the self-diffusivities of both nC6 and 2MP in C6/ 2MP mixtures. These measurements were made at a total loading that is kept nearly constant at 3.5 molecules per unit cell. Their data, that were measured at 433 K and re-plotted in Figure 19a, shows that *both* self-diffusivities are reduced with increasing loading of 2MP in the mixture. The preferential location of 2MP at the intersections causes blocking of molecular traffic in the intersecting channel system of MFI. We also note that the linear nC6 has a diffusivity that is about an order of magnitude higher than that of the branched 2MP.

Figure 19b presents the data on the ratio of the self-diffusivity of nC6 to that of 2MP. With increased 2MP loading, the diffusivity of nC6 increases far more significantly than that of 2MP. This implies that there are no slowing-down effects of nC6 due to the presence of the tardier 2MP. Rather, there is an enhancement of the mobility of nC6 with increased loading. Put another way, when analysing mixture diffusion of hexane isomer mixtures correlation effects can be ignored as a *conservative* estimate. The diffusion of nC6/2MP mixture in MFI has very special and unusual characteristics; nC6 is much more mobile, by about one order of magnitude. Furthermore, as a consequence of configurational entropy effects, the more strongly adsorbed species is also nC6. We therefore have a mixture of more-mobile-

more-strongly-adsorbed-nC6 and tardier-less-strongly-adsorbed-2MP. There is unusual synergy between adsorption and diffusion of alkane isomers in MFI zeolite.

We now demonstrate that correlation effects are unlikely to be significant for nC6/2MP uptake in MFI. In light of the experimental data presented in Figure 19c, we may assume that both $Đ_1$ and $Đ_2$ decrease to the same extent with increased loading of 2MP. Assuming the ratios ($Đ_1/Đ_2$) and ($Đ_1/Đ_{12}$) to be *independent* of loading, the impact of correlations are quantified by the ratios of the off-diagonal elements to the main elements of $\begin{bmatrix} \Delta_{11} & \Delta_{12} \\ \Delta_{21} & \Delta_{21} \end{bmatrix}$, i.e.

$$\frac{\Delta_{12}}{\Delta_{11}} = \frac{\frac{x_1 Đ_2}{Đ_{12}}}{\left(1+\frac{x_1 Đ_2}{Đ_{12}}\right)} \tag{30}$$

and

$$\frac{\Delta_{21}}{\Delta_{21}} = \frac{\frac{x_2 Đ_1}{Đ_{12}}}{\left(1+\frac{x_2 Đ_1}{Đ_{12}}\right)} \tag{31}$$

Figure 20 presents calculations of the ratios $\frac{\Delta_{12}}{\Delta_{11}}$, and $\frac{\Delta_{21}}{\Delta_{21}}$ for nC6/2MP mixture diffusion for the parameters ($Đ_1/Đ_2$) = 100 and ($Đ_1/Đ_{12}$) =1. The chosen ratio ($Đ_1/Đ_2$) = 100 is based on the results to be presented in a later section on modelling the IRM uptake experiments. The value of ($Đ_1/Đ_{12}$) = 1 can be regarded as reflecting a reasonably high degree of correlation.[33]

We note that for nC6 the contribution of the off-diagonal element is likely to be less than 1%. For 2MP, the contribution of the off-diagonal element is likely to be in the range of 6 - 20% for the range of operating conditions that prevail in the IRM uptake experiments modeled in this paper.

In view of the foregoing arguments, we proceed further in modeling the uptake experiments by ignoring the off-diagonal elements and adopting the following set of flux equations

$$\begin{pmatrix} N_1 \\ N_2 \end{pmatrix} = -\rho \begin{bmatrix} Đ_1 & 0 \\ 0 & Đ_2 \end{bmatrix} \begin{bmatrix} \Gamma_{11} & \Gamma_{12} \\ \Gamma_{21} & \Gamma_{21} \end{bmatrix} \frac{\partial \begin{pmatrix} q_1 \\ q_2 \end{pmatrix}}{\partial r} \tag{32}$$

11. Simulation methodology of transient uptake in MFI crystal

For most crystal geometries, representation as an equivalent sphere is an acceptable approximation as argued by Ruthven.[36] Indeed, most researchers report their uptake diffusivities in terms of a model that assumes uptake within a single spherical crystalline particle. The values thus obtained for the diffusivities within a spherical crystal can be translated to other crystal geometries by comparing values at the same characteristic dimension, defined as the ratio of the crystal volume to its external suface area. For a spherical shaped crystal of radius r_c, the ratio of the volume to the external surface area is $\frac{\left(\frac{4}{3}\pi r_c^3\right)}{4\pi r_c^2} = \frac{r_c}{3}$. For a cylindrical shaped crystal of radius r_c and length L, the ratio of the volume to the external surface area is $\frac{\left(\pi r_c^2 L\right)}{2\pi r_c L + 2\pi r_c^2}$, which reduces to $\frac{r_c}{2}$ for an infinitely long cylinder. For a cuboid crystal of dimensions a, b, and c, the volume to surface area ratio is $\frac{(abc)}{2(ab+bc+ca)}$. The formula for cuboids is applicable to coffin-shaped MFI crystals. The mathematical analysis developed below for spherical crystals of radius r_c, may be applied to coffin-shaped MFI crystals by taking an equivalent radius of sphere to be $\frac{3(abc)}{2(ab+bc+ca)}$. For the IRM measurements, with coffin-shaped crystals with dimensions of 25 μm x 25 μm x 180 μm the equivalent radius of a spherical crystal is r_c = 17.6 μm.

The radial distribution of molar loadings, q_i, within a spherical MFI crystallite, of radius r_c, is obtained from a solution of a set of differential equations describing the uptake

$$\frac{\partial q_i(r,t)}{\partial t} = -\frac{1}{\rho}\frac{1}{r^2}\frac{\partial}{\partial r}\left(r^2 N_i\right) \tag{33}$$

The fluxes N_i, in turn, are related to the radial gradients in the molar loadings by equation (32). At time $t = 0$, i.e. the initial conditions, the molar loadings $q_i(r,0)$ at all locations r within the crystal are uniform. For all times $t \geq 0$, the exterior of the crystal is brought into contact with a bulk gas mixture at a different $p_i(r_c,t)$ that is maintained constant till the crystal reaches thermodynamic equilibrium with the surrounding gas mixture.

$$t \geq 0; \quad q_i(r_c,t) \text{ in equilibrium with the initial values } p_i(r_c,t) \tag{34}$$

At any time t, during the transient approach to thermodynamic equilibrium, the spatially averaged molar loading within the crystallites of radius r_c is calculated using

$$\bar{q}_i(t) = \frac{3}{r_c^3}\int_0^{r_c} q_i(r,t) r^2 dr \tag{35}$$

The $\bar{q}_i(t)$ can be compared directly with experimental transient uptake data.

An analytical solution to equation (33) is only possible for the special case of unary diffusion (cf. equation (18)) in which the Fick diffusivity, D_i, defined in equation (19), can be considered to be independent of the loading. The expression for fractional approach to equilibrium is[34]

$$\frac{\left(\bar{q}_i(t) - q_i(r_c,0)\right)}{\left(q_i(r_c,t=\infty) - q_i(r_c,0)\right)} = 1 - \frac{6}{\pi^2}\sum_{m=1}^{\infty}\frac{\exp(-m^2\pi^2\frac{D_i}{r_c^2}t)}{m^2} \tag{36}$$

There is no generally applicable analytical solution to describe transient diffusion of binary mixtures and the set of equations (32), (33), and (34) need to be solved numerically using robust computational techniques. Equations (33) are first subjected to finite volume discretization. The choice of the discretization scheme used is crucially important in obtaining accurate, converged results. Each crystallite, assumed to be spherical, is divided into equi-volume slices as sketched in Figure 21. The choice of equi-volume slices instead of equi-distant slices of the spherical particle is dictated by the fact that the gradients of the loadings are particularly steep nearer to $r = r_c$. To illustrate the steepness of the gradients, Figure 22 presents calculations of the radial profiles of the loadings of nC6 and 2MP within

MFI crystal for conditions corresponding to Run 1 (discussed in detail in the following section, with data inputs as specified in the legend to Figure 23), monitored at times (a) t = 1.23 s, (b) t = 5 s, (c) t = 10.2 s, (d) t = 50.6 s, and (e) t = 832 s. For times t < 10 s, we note that the nC6 loadings exhibit a maximum in the loading at a position $r/ r_c \approx 0.9$. Computationally, it is much more efficient to use more slices in the outer regions ($0.8 < r/ r_c < 1$) and fewer slices in the central core regions ($0 < r/ r_c < 0.8$). For the simulations of Runs 1, 2, 3, and 4 discussed below, we found that 300-500 equi-volume slices within each crystallite need to be used for good accuracy and to ensure convergence. The number of slices is much larger than in more common applications where accurate results are ensured with only 20 slices.

Further details of the numerical procedures used in this work, are provided by Krishna and co-workers;[11, 34, 37]

12. Comparison of simulations with transient IRM uptake

Each of the four IRM experiments for uptake of nC6/2MP mixtures was simulated separately. In all four runs the bulk gas mixture was equimolar ($p_1 = p_2$) and maintained at constant temperature of 298 K. Each of these Runs are discussed below in turn.

In Run 1, the initially virgin MFI crystal is exposed to a gas mixture at p_t = 2.6 Pa. For understanding of the transient uptake, Figure 23a presents the CBMC data for mixture adsorption with indication of the range of loadings involved for the pressure step 0 – 2.6 Pa used. Both nC6 and 2MP loadings increase in the IRM experiments till equilibration is reached. The essential features of the transient uptake can be adequately simulated by choosing : $Đ_1/r_c^2 = 0.016$ s^{-1}; $Đ_2/r_c^2 = 1.6\times10^{-4}$ s^{-1}; both values are assumed to be constant for the loading range encountered in Run 1. Particularly noteworthy is that the experimentally observed overshoot of nC6 uptake is adequately reflected in the simulations; see Figure 23b. The total mixture loading at which the maximum in the nC6 uptake occurs is $\Theta_t \approx 4$ molecules/uc. As shown in Figure 18c, the value of $(\Gamma_{12}\,\Theta_2/\Gamma_{11}\,\Theta_1)$ exhibits a maximum at $\Theta_t \approx 4$ molecules/uc. The inescapable conclusion is that the maximum in $(\Gamma_{12}\,\Theta_2/\Gamma_{11}\,\Theta_1)$ is directly

contributory to the maximum in the corresponding uptake in the simulation. Indeed, to confirm that the characteristics of the matrix $\begin{bmatrix} \Gamma_{11} & \Gamma_{12} \\ \Gamma_{21} & \Gamma_{21} \end{bmatrix}$ causes the overshoot, we carried out simulations in which this correction factor is assumed to be the identity matrix, and the following, simplified, flux relations apply

$$\begin{pmatrix} N_1 \\ N_2 \end{pmatrix} = -\rho \begin{bmatrix} Đ_1 & 0 \\ 0 & Đ_2 \end{bmatrix} \begin{bmatrix} 1 & 0 \\ 0 & 1 \end{bmatrix} \frac{\partial \begin{pmatrix} q_1 \\ q_2 \end{pmatrix}}{\partial r}; \quad \text{no thermodynamic coupling} \tag{37}$$

Figure 23c shows transient simulations using the simplified equation (37). In this case no overshoot is detected in nC6 uptake, demonstrating incontrovertibly that the nC6 overshoot is ascribable to thermodynamic coupling.

For Run 2, the initial conditions correspond to the final equilibrated loadings of Run 1. In Run 2 the pressure is increased to 4 Pa. The pressure step from 2.6 Pa to 4 Pa is a crucial one as it signifies the onset of configurational entropy effects as indicated in the CBMC mixture simulation data in Figure 24a. The 2MP loading is anticipated to decrease, albeit slightly, due to loss of the entropy battle with nC6. This slight decrease is witnessed in the IRM experimental data. The IRM experiments can be adequately simulated by choosing: $Đ_1/r_c^2 = 0.02$ s^{-1}; $Đ_2/r_c^2 = 2\times10^{-4}$ s^{-1}; both values are assumed to be constant for the loading range encountered in Run 2.

For Run 3, the initial conditions correspond to the final equilibrated loadings of Run 2. In Run 3 the pressure is increased to 12.2 Pa. For the pressure step from 4 Pa to 12.2 Pa, entropy effects significantly impact on 2MP, and cause its exclusion from the MFI crystals as indicated in the CBMC mixture simulation data in Figure 25a. The exclusion of 2MP due to entropy effects is reflected in the IRM experimental data The IRM experiments can be adequately simulated by choosing: $Đ_1/r_c^2 = 0.04$ s^{-1}; $Đ_2/r_c^2 = 4\times10^{-4}$ s^{-1}; both values are assumed to be constant for the loading range encountered in Run 4.

For Run 4, the initial conditions correspond to the final equilibrated loadings of Run 3. In Run 4 the pressure is increased to 102 Pa. For the pressure step from 12.2 Pa to 102 Pa, entropy effects also significantly impact on 2MP, and cause its exclusion from the MFI crystals as indicated in the CBMC

mixture simulation data in Figure 26a. The exclusion of 2MP due to entropy effects is reflected in the IRM experimental data The IRM experiments can be adequately simulated by choosing: $Đ_1/r_c^2$ = 0.16 s^{-1}; $Đ_2/r_c^2$ = 1.6×10^{-3} s^{-1}; both values are assumed to be constant for the loading range encountered in Run 4.

Having established that the Maxwell-Stefan flux equations (32), neglecting correlation effects, is of adequate accuracy to describe the transient uptake for all four Runs 1, 2, 3 and 4, we now seek confirmation that this neglect is indeed justified. For this purpose, we carried out transient uptake simulations using the using Equations (20), (21), and (22). For estimation of the exchange coefficient, $Đ_{12}$, we use the interpolation formula[38]

$$Đ_{12} = (Đ_1)^{x_1}(Đ_2)^{x_2} \tag{38}$$

The interpolation formula (38) has been validated with the aid of Molecular Dynamics (MD) simulations.[38] Figure 26c demonstrates that the simulations including correlation effects yields transient uptake profiles that are practically indistinguishable from those obtained using the simplified equations (32); this finding was already anticipated in the foregoing section in the context of the results presented in Figure 20.

Figures 27a, and 27b present a summary comparison demonstrating the one-to-one correspondence between nC6/2MP mixture adsorption and transient nC6/2MP mixture uptake data. The maximum in the 2MP loading observed in the CBMC mixture simulations causes the 2MP loadings in the Runs 2, 3, and 4 to decrease, while the partial pressures of 2MP in the bulk gas mixture are progressively ramped upwards. Figure 27b also shows that the use of the Maxwell-Stefan model, with flux equations described by equations (32), have the ability to capture the all of the essential features of the nC6/2MP mixture uptake observed in the IRM experiments, including the nC6 overshoot in Run 1.

Let us examine the trends in the fitted values of the Maxwell-Stefan diffusivities used in each of the four runs in order to match the IRM experiments. Figure 28 presents a plot of the fitted diffusivity values, $Đ_1/r_c^2$, and $Đ_2/r_c^2$ as a function of the 2MP loading. The chosen loading correspond to the

values at the end of the equilibration of each of the four runs. We note that both diffusivities decrease in a similar fashion as the 2MP loading increases from 0 to 2 molecules per unit cell. This trend is remarkably similar to that observed in the self-diffusivity data for nC6 and 2MP in MFI at 433 K; see Figure 19c. The transient uptake of nC6/2MP mixtures clearly demonstrates that the blocking of intersections of MFI by 2MP has a significant impact on the diffusivities of both nC6 and 2MP.

For the coffin-shaped MFI crystals used in the IRM experiments, insertion of the effective sphere radius, r_c = 18.08 μm yields the diffusivity values of nC6 and 2MP.

Figure 29 present simulation results for transient desorption kinetics for nC6/2MP mixture adsorbed in MFI, subjected to a step decrease in total pressure of the surrounding gas phase. Simulations including thermodynamic coupling (continuous solid lines) show a small undershoots for the more mobile nC6. If thermodynamic coupling effects are ignored, no undershoot is detected. There is no experimental verification of undershoot phenomena in the published literature.

13. Other examples of overshoots in transient uptake

Figure 30 presents simulations of the transient uptake of nC4/iC4 mixture in MFI using the Maxwell-Stefan model with flux equations (32). The more mobile nC4 exhibits an overshoot during the early stages of the transience, analogous to the observations for nC6/2MP mixtures in Run 1. These simulations are reported here just to underscore the fact that overshoots are not the exclusive domain of nC6/2MP mixtures. Several other examples of overshoots in the mobile partner species have been reported in the literature; a careful analysis of these experimental data demonstrates that in all cases such overshoots are ascribable to thermodynamic coupling.[11] These findings are in line with those reached in the experimental study reported here.

Krishna[11] has shown that the overshoots of the more mobile partners in the uptake of N_2/CH_4 in LTA-4A, [39] benzene/p-xylene in ZSM-5, [40, 41] benzene/ethylbenzene in ZSM-5,[40, 41] CH_4/C_2H_6 in LTA-4A,[42] n-heptane/benzene in NaX, [43] ethanol/1-propanol in SAPO-34,[44] and methanol/1-propanol in SAPO-34,[44] methanol/ethanol in SAPO-34[44] is the direct result of thermodynamic coupling effects in mixture diffusion.

14. Conclusions

Infra-Red Microscopy (IRM) measurements have been used in this work to demonstrate the strong influence of configurational entropy effects of adsorption and diffusion of mixtures of nC4(1)/iC4(2) and nC6(1)/2MP(2) in MFI zeolite. The following major conclusions emerge from this study.

(1) With increasing total pressure, $p_t = p_1 + p_2$, of an equimolar gas mixture ($p_1 = p_2$), the adsorbed loadings of the branched isomer, Θ_2 , decreases when conditions are such that $\Theta_t = \Theta_1 + \Theta_2 > 4$ molecules per unit cell

(2) For mixture loadings $\Theta_t > 4$ per uc, the adsorption selectivity S_{ads} is strongly in favor of the linear isomer

(3) For transient uptake of nC6(1)/2MP(2) mixture, the 2MP uptake decreases with increasing total pressure for conditions in which the adsorbed loading $\Theta_t = \Theta_1 + \Theta_2 > 4$ molecules per unit cell. This phenomenon is quantitatively captured by the Maxwell-Stefan flux equations (32), that ignores correlation effects.

(4) One major conclusion that emerges from this study is the synergism between configurational entropy effects on mixture adsorption equilibrium and the attendant intersection blocking effects on mixture diffusion. Entropy effects tend to suppress the adsorption of the branched isomer 2MP. This suppression has the net effect of reducing the extent of intersection blocking. Consequently, the diffusivities of nC6 increases; see Figure 28.

15. Acknowledgements

The authors are grateful to Wolfgang Schmidt for providing MFI crystals used in the IRM experiments.

16. Notation

b_A	dual-Langmuir-Freundlich constant for species *i* at adsorption site A, $Pa^{-\nu_i}$
b_B	dual-Langmuir-Freundlich constant for species *i* at adsorption site B, $Pa^{-\nu_i}$
$[B]$	matrix of inverse M-S coefficients, defined by eq. (13), m^{-2} s
$Đ_i$	Maxwell-Stefan diffusivity, m^2 s^{-1}
$Đ_{ij}$	M-S exchange coefficient, m^2 s^{-1}
D_i	Fick diffusivity of species *i*, m^2 s^{-1}
$Đ_{ij}$	M-S exchange coefficient, m^2 s^{-1}
$D_{i,self}$	self-diffusivity of species *i*, m^2 s^{-1}
f_i	partial fugacity of species *i*, Pa
f_t	total fugacity of bulk fluid mixture, Pa
m	summation index, dimensionless
n	number of species in the mixture, dimensionless
N_i	molar flux of species *i*, mol m^{-2} s^{-1}
p_i	partial pressure of species *i* in mixture, Pa
p_t	total system pressure, Pa
P_i^0	sorption pressure, Pa
q_i	component molar loading of species *i*, mol kg^{-1}
$q_i^0(f)$	pure component adsorption isotherm of species *i*, mol kg^{-1}
$q_{i,sat}$	molar loading of species *i* at saturation, mol kg^{-1}
q_t	total molar loading in mixture, mol kg^{-1}
$q_{sat,A}$	saturation loading of site A, mol kg^{-1}
$q_{sat,B}$	saturation loading of site B, mol kg^{-1}
$\bar{q}_i(t)$	*spatially averaged* component molar loading of species *i*, mol kg^{-1}
r	radial direction coordinate, m

r_c	radius of crystallite, m
R	gas constant, 8.314 J mol^{-1} K^{-1}
S_{ads}	adsorption selectivity, dimensionless
t	time, s
T	absolute temperature, K
x_i	mole fraction of species *i* in adsorbed phase, dimensionless
y_i	mole fraction of component *i* in bulk vapor phase, dimensionless

Greek letters

δ_{ij}	Kronecker delta, dimensionless
$[\Delta]$	matrix defined of M-S diffusivities, m^2 s^{-1}
Δ_{ij}	elements of $[\Delta]$, m^2 s^{-1}
γ_i	activity coefficient of component *i* in adsorbed phase, dimensionless
Γ_{ij}	thermodynamic factors, dimensionless
$[\Gamma]$	matrix of thermodynamic factors, dimensionless
Φ	surface potential of adsorbed mixture, J m^{-3}
Φ_i^0	surface potential of pure component *i* in adsorbed phase i, J m^{-3}
Λ_{ij}	Wilson parameters defined by Equation (10), dimensionless
μ_i	molar chemical potential, J mol^{-1}
ν	exponent in dual-Langmuir-Freundlich isotherm, dimensionless
μ_i	molar chemical potential, J mol^{-1}
θ_i	fractional occupancy of component *i*, dimensionless
Θ_i	loading of species *i*, molecules per unit cell
$\Theta_{I,sat}$	saturation loading of species *i*, molecules per unit cell
Θ_t	total molar loading of mixture, molecules per unit cell
ρ	framework density, kg m^{-3}

Subscripts

i	referring to component *i*
A	referring to site A
B	referring to site B
t	referring to total mixture

Table 1. Dual-site Langmuir-Freundlich parameters for pure component isotherms in MFI at 298 K.

	Site A			Site B		
	$\Theta_{i,A,sat}$ molecules uc^{-1}	$b_{i,A}$ Pa$^{-\nu_i}$	$\nu_{i,A}$ dimensionless	$\Theta_{i,B,sat}$ molecules uc^{-1}	$b_{i,B}$ Pa$^{-\nu_i}$	$\nu_{i,B}$ dimensionless
nC_4H_{10}	1.5	2.24×10^{-3}	0.57	8.7	9.75×10^{-3}	1.12
iC_4H_{10}	4	2.29×10^{-2}	1	6	2.87×10^{-5}	1

Table 2. Dual-site Langmuir-Freundlich parameters for pure component isotherms in MFI at 298 K.

	Site A			Site B		
	$\Theta_{i,A,sat}$ molecules uc^{-1}	$b_{i,A}$ Pa$^{-\nu_i}$	$\nu_{i,A}$ dimensionless	$\Theta_{i,B,sat}$ molecules uc^{-1}	$b_{i,B}$ Pa$^{-\nu_i}$	$\nu_{i,B}$ dimensionless
nC6	6.6	0.708	0.83	1.4	16.6	1.5
2MP	4	4.51	1.05	4	7.92×10^{-6}	1.13

Table 3. Wilson non-ideality parameters for nC4/iC4 and nC6/2MP mixtures at 298 K.

	Λ_{12}	Λ_{21}
nC4/iC4 mixture	3	1.1
nC6/2MP mixture	1.05	0.2

17. References

(1) Griffiths, P. R.; de Haseth, J. A. Fourier Transform Infrared Spectrometry John Wiley & Sons Inc.: New York, 1986.

(2) Bell, R. G. Introductory Fourier Transform Spectroscopy; Academic Press: New York, 1972.

(3) Chmelik, C.; Bux, H.; Caro, J.; Heinke, L.; Hibbe, F.; Titze, T.; Kärger, J. Mass transfer in a Nanoscale Material Enhanced by an Opposing Flux, *Phys. Rev. Lett.* **2010**, *104*, 085902.

(4) Chmelik, C.; Heinke, L.; Kärger, J.; Shah, D. B.; Schmidt, W.; van Baten, J. M.; Krishna, R. Inflection in the Loading Dependence of the Maxwell-Stefan Diffusivity of Iso-butane in MFI Zeolite, *Chem. Phys. Lett.* **2008**, *459*, 141-145.

(5) Chmelik, C.; Kärger, J.; Wiebcke, M.; Caro, J.; van Baten, J. M.; Krishna, R. Adsorption and Diffusion of Alkanes in CuBTC Crystals Investigated Using Infrared Microscopy and Molecular Simulations, *Microporous Mesoporous Mater.* **2009**, *117*, 22-32.

(6) Chmelik, C.; Heinke, L.; van Baten, J. M.; Krishna, R. Diffusion of *n*-butane/*iso*-butane Mixtures in Silicalite-1 Investigated Using Infrared (IR) Microscopy, *Microporous Mesoporous Mater.* **2009**, *125*, 11-16.

(7) Heinke, L.; Chmelik, C.; Kortunov, P.; Shah, D. B.; Brandani, S.; Ruthven, D. M.; Kärger, J. Analysis of thermal effects in infrared and interference microscopy: *n*-Butane-5A and methanol–ferrierite systems, *Microporous Mesoporous Mater.* **2007**, *104*, 18-25.

(8) Schmidt, W.; Wilczok, U.; Weidenthaler, C.; Medenbach, O.; Goddard, R.; Buth, G.; Cepak, A. Preparation and Morphology of Pyramidal MFI Single-Crystal Segments, *J. Phys. Chem. B* **2007**, *111*, 13538-13543.

(9) Dubbeldam, D.; Calero, S.; Vlugt, T. J. H.; Krishna, R.; Maesen, T. L. M.; Smit, B. United Atom Forcefield for Alkanes in Nanoporous Materials, *J. Phys. Chem. B* **2004**, *108*, 12301-12313.

(10) Dubbeldam, D.; Krishna, R.; Calero, S.; Yazaydın, A. Ö. Computer-Assisted Screening of Ordered Crystalline Nanoporous Adsorbents for Separation of Alkane Isomers, *Angew. Chem. Int. Ed.* **2012**, *51*, 11867-11871.

(11) Krishna, R. The Maxwell-Stefan Description of Mixture Diffusion in Nanoporous Crystalline Materials, *Microporous Mesoporous Mater.* **2014**, *185*, 30-50.

(12) Vlugt, T. J. H.; Krishna, R.; Smit, B. Molecular Simulations of Adsorption Isotherms for Linear and Branched Alkanes and Their Mixtures in Silicalite, *J. Phys. Chem. B* **1999**, *103*, 1102-1118.

(13) Frenkel, D.; Smit, B. Understanding Molecular Simulations: From Algorithms to Applications; 2nd Edition, Academic Press: San Diego, 2002.

(14) Siepmann, J. I.; Martin, M. G.; Mundy, C. J.; Klein, M. L. Intermolecular potentials for branched alkanes and the vapour-liquid phase equilibria of n-heptane, 2-methylhexane, and 3-ethylpentane, *Mol. Phys.* **1997**, *90*, 687-693.

(15) Bezus, A. G.; Kiselev, A. V.; Lopatkin, A. A.; Du, P. Q. Molecular statistical calculation of the thermodynamic adsorption characteristics of zeolites using the atom-atom approximation. Part 1. Adsorption of methane by zeolite sodium-X, *J.Chem.Soc., Faraday Trans. II* **1978**, *74*, 367-379.

(16) Baerlocher, C.; Meier, W. M.; Olson, D. H. Atlas of Zeolite Framework Types; 5th Edition, Elsevier: Amsterdam, 2002.

(17) Sun, M. S.; Shah, D. B.; Xu, H. H.; Talu, O. Adsorption equilibria of C_1 to C_4 alkanes, CO_2, and SF_6 on silicalite, *J. Phys. Chem. B* **1998**, *102*, 1466-1473.

(18) Zhu, W.; Kapteijn, F.; Moulijn, J. A. Equilibrium adsorption of light alkanes in silicalite-1 by the inertial microbalance technique, *Adsorpt.-J. Int. Adsorpt. Soc.* **2000**, *6*, 159-167.

(19) Song, L.; Rees, L. V. C. Adsorption and transport of n-hexane in siliaclite-1 by the frequency response technique, *J. Chem. Soc.-Faraday Trans.* **1997**, *93*, 649-657.

(20) Millot, B.; Méthivier, A.; Jobic, H.; Clemencon, I.; Rebours, B. Adsorption of branched alkanes in silicalite-1: A temperature- programmed-equilibration study, *Langmuir* **1999**, *15*, 2534-2539.

(21) Millot, B.; Méthivier, A.; Jobic, H. Adsorption of n-alkanes on silicalite crystals. A temperature- programmed desorption study, *J. Phys. Chem. B* **1998**, *102*, 3210-3215.

(22) Sun, M. S.; Talu, O.; Shah, D. B. Adsorption equilibria of C_5 - C_{10} normal alkanes in silicalite crystals, *J. Phys. Chem.* **1996**, *100*, 17276-17280.

(23) Eder, F. Thermodynamics and siting of alkane sorption in molecular sieves, Ph.D. Dissertation, Universiteit Twente, Enschede, 1996

(24) Zhu, W.; Kapteijn, F.; van der Linden, B.; Moulijn, J. A. Equilibrium adsorption of linear and branched C_6 alkanes on silicalite-1 studied by the tapered element oscillating microbalance, *Phys. Chem. Chem. Phys.* **2001**, *3*, 1755-1761.

(25) Vlugt, T. J. H.; Zhu, W.; Kapteijn, F.; Moulijn, J. A.; Smit, B.; Krishna, R. Adsorption of linear and branched alkanes in the silicalite-1, *J. Am. Chem. Soc.* **1998**, *120*, 5599-5600.

(26) Jolimaître, E.; Tayakout-Fayolle, M.; Jallut, C.; Ragil, K. Determination of mass transfer and thermodynamic properties of branched paraffins in silicalite by inverse chromatography technique, *Ind. Eng. Chem. Res.* **2001**, *40*, 914-926.

(27) Krishna, R.; Smit, B.; Vlugt, T. J. H. Sorption-induced Diffusion-selective Separation of Hydrocarbon Isomers Using Silicalite, *J. Phys. Chem. A* **1998**, *102*, 7727-7730.

(28) Myers, A. L.; Prausnitz, J. M. Thermodynamics of mixed gas adsorption, *A.I.Ch.E.J.* **1965**, *11*, 121-130.

(29) Krishna, R.; Paschek, D. Molecular simulations of adsorption and siting of light alkanes in silicalite-1, *Phys. Chem. Chem. Phys.* **2001**, *3*, 453-462.

(30) Calleja, G.; Jimenez, A.; Pau, J.; Domínguez, L.; Pérez, P. Multicomponent adsorption equilibrium of ethylene, propane, propylene and CO, on 13X zeolite, *Gas Sep. Purif.* **1994**, *8*, 247-256.

(31) Krishna, R. Describing the diffusion of guest molecules inside porous structures, *J. Phys. Chem. C* **2009**, *113*, 19756-19781.

(32) Krishna, R. Diffusion in Porous Crystalline Materials, *Chem. Soc. Rev.* **2012**, *41*, 3099-3118.

(33) Krishna, R.; van Baten, J. M. Investigating the Influence of Diffusional Coupling on Mixture Permeation across Porous Membranes *J. Membr. Sci.* **2013**, *430*, 113-128.

(34) Krishna, R.; Baur, R. Modelling issues in zeolite based separation processes, *Sep. Purif. Technol.* **2003**, *33*, 213-254.

(35) Schuring, D.; Jansen, A. P. J.; van Santen, R. A. Concentration and chainlength dependence of the diffusivity of alkanes in zeolites studied with MD simulations, *J. Phys. Chem. B* **2000**, *104*, 941-948.

(36) Ruthven, D. M. Principles of Adsorption and Adsorption Processes; John Wiley: New York, 1984.

(37) Krishna, R.; van Baten, J. M. Investigating the potential of MgMOF-74 membranes for CO_2 capture, *J. Membr. Sci.* **2011**, *377*, 249-260.

(38) Krishna, R. Verification of the Maxwell-Stefan theory for mixture diffusion in zeolites by comparison with MD simulations, *Chem. Eng. J.* **2001**, *84*, 207-214.

(39) Habgood, H. W. The Kinetics of Molecular Sieve Action. Sorption of Nitrogen-Methane Mixtures by Linde Molecular Sieve 4A, *Canad. J. Chem.* **1958**, *36*, 1384-1397.

(40) Niessen, W.; Karge, H. G. Diffusion of *p*-xylene in Single and Binary Systems Investigated by FTIR Spectroscopy, *Microporous Mater.* **1993**, *1*, 1-8.

(41) Karge, H. G. Infrared Spectroscopic Investigation of Diffusion, Co-diffusion and Counter-diffusion of Hydrocarbon Molecules in Zeolites, *C.R. Chim.* **2005**, *8*, 303-319.

(42) Carlson, N. W.; Dranoff, J. S. Competitive adsorption of methane and ethane on 4A zeolite. Fundamentals of Adsorption; Edited by A.I. Liapis, AIChE: New York, 1986.

(43) Kärger, J.; Bülow, M. Theoretical Prediction of Uptake Behaviour in Adsorption Kinetics of Binary Gas Mixtures Using Irreversible Thermodynamics, *Chem. Eng. Sci.* **1975**, *30*, 893-896.

(44) Saint-Remi, J. C.; Baron, G. V.; Denayer, J. F. M. Non-Uniform Chain Length Dependent Diffusion of Short 1-Alcohols in SAPO-34 in Liquid Phase, *J. Phys. Chem. C* **2013**, *117*, 9758-9765.

(45) Cavalcante, C. L.; Ruthven, D. M. Adsorption of Branched and Cyclic Paraffins in Silicalite .1. Equilibrium, *Ind. Eng. Chem. Res.* **1995**, *34*, 177-184.

18. Caption for Figures

Figure 1. IR Microscopy (IRM) – Experimental setup. Photograph of the IRM microscope including a close-up view of the motorized platform with optical cell. The upper-right picture shows the silicalite-1 crystal observed with the microscope operated in the viewing mode. The crystal is framed by the rectangular aperture (only part in the centre is transparent for IR light).

Figure 2. Measurement of integral uptake curves with the single element detector. (a) Absorption spectra were recorded in the IR-transmission mode of the microscope with a temporal resolution between 0.3 – 1.5 s. (b) Changes in guest concentration were determined by calculating the changes in the area under characteristic IR bands. (c)Plotting the time evolution of the normalized band intensity gives the integral "uptake curve" which can be analysed by an appropriate solution of Fick's second law to obtain the diffusivity.

Figure 3. Channel dimensions of MFI zeolite.

Figure 4. CBMC simulations of pure component isotherms for CH_4 (= C1), C_2H_6 (= C3), and C_3H_8 (= C3) at a variety of temperatures compared with the experimental data of Sun et al.[17] Also shown is snapshot of nC4 molecules within the straight and zig-zag channels of MFI at a total loading of 4 molecules per unit cell.

Figure 5. Comparison of CBMC simulations of pure component isotherms for nC_4H_{10} (= nC4) with the experimental data of with the experimental data of Sun et al.[17] and Zhu et al.[18] The CBMC simulations for nC4 at 298 K are fitted with the dual-Langmuir-Freundlich parameters specified in Table 1. Also shown are snapshot of nC4 molecules within the straight and zig-zag channels of MFI at a total loading of 4 molecules per unit cell.

Figure 6. Comparison of experimental isotherm data of Song and Rees [19] and Millot et al.[20, 21] with CBMC simulations for nC6 at a variety of temperatures.

Figure 7. Comparison of CBMC simulations of pure component isotherm for n-heptane (= nC7) compared with the experimental data of Sun et al.[22] and Eder.[23] Also shown is snapshot of nC7 molecules at a total loading of 4 molecules per unit cell.

Figure 8. Comparison of CBMC simulations of pure component isotherms for iC_4H_{10} (= iC4) at a variety of temperatures compared with the experimental data of Sun et al.[17] and Zhu et al.[18] The CBMC simulations for iC4 at 298 K are fitted with the dual-Langmuir-Freundlich parameters specified in Table 1. Also shown is snapshot of iC4 molecules at a total loading of 4 molecules per unit cell.

Figure 9. CBMC simulations of pure component isotherm for 2-methylpentane (= 2MP) compared with experimental isotherm data of Zhu et al.[24] at 303 K. The CBMC simulations for 2MP are fitted with the dual-Langmuir-Freundlich parameters specified in Table 2. Also shown is snapshot of 2MP molecules.

Figure 10. Comparison of CBMC simulations of pure component isotherm for 3-methylpentane (= 3MP) with the experimental data of Zhu et al.[24] and Jolimaître et al.[26] Also shown is snapshot of 3MP molecules.

Figure 11. CBMC simulations of pure component isotherms for 2,2 dimethylbutane (= 22DMB) and 2,3 dimethylbutane (23DMB). Also shown are comparisons with the experimental data of Cavalcante and Ruthven.[45] Also shown are snapshots of 22DMB molecules adsorbed in MFI. The CBMC simulations for 22DMB are fitted with the dual-Langmuir-Freundlich parameters specified in Table 2.

Figure 12. The experimental IRM isotherm data for nC6 at 298 K determined in this work are compared with the corresponding CBMC simulations for nC6; the CBMC data are fitted with the dual-Langmuir-Freundlich parameters specified in Table 2. Also shown are snapshots showing the location of nC6 molecules within the straight and zig-zag channels of MFI.

Figure 13. CBMC simulations of pure component isotherm for 2-methylpentane (= 2MP) compared with the IRM experimental data at 298 K. The CBMC simulations for 2MP are fitted with the dual-Langmuir-Freundlich parameters specified in Table 2. Also shown are snapshots of 2MP molecules.

Figure 14. (a, b) CBMC simulations of loadings in the adsorbed phase in equilibrium with binary nC6/2MP mixture with partial pressures $p_1 = p_2$ in the bulk gas phase at 298 K. Also shown are IRM experimental data. (c) Calculations of the adsorption selectivity, S_{ads}, using Equation (3). (c) Snapshot showing the location of nC6 (Θ_1 = 2/uc) and 2MP (Θ_2 = 2/uc) molecules at a total loading Θ_t = 4/uc.

Figure 15. (a) CBMC simulations of loadings in the adsorbed phase in equilibrium with binary nC4/iC4 mixture with partial pressures $p_1 = p_2$ in the bulk gas phase at 298 K. Also shown are IRM experimental data. (b) Calculations of the adsorption selectivity, S_{ads}, using Equation (3). Snapshots showing the location of nC4 (Θ_1 = 2/uc) and iC4 (Θ_2 = 2/uc) molecules at a total loading Θ_t = 4/uc.

Figure 16. Comparison of the estimations using the Ideal Adsorbed Solution Theory (IAST) with CBMC simulations of component loadings of binary (a) nC4/iC4, and (b) nC6/2MP mixtures.

Figure 17. Comparison of the estimations using the Real Adsorbed Solution Theory (RAST)[30] with CBMC simulations of component loadings of binary (a) nC4/iC4, and (b) nC6/2MP mixtures. The activity coefficient describing the non-ideality of the adsorbed mixture is described by Equation (10), with the Wilson non-ideality parameters for nC4/iC4 and nC6/2MP mixtures as specified in Table 3.

Figure 18. (a) Calculations of the elements Γ_{ij} of the thermodynamic corrector factor matrix [Γ] for nC6/2MP mixture as a function of the bulk gas phase fugacity at 298 K, with partial pressures $p_1 = p_2$. (b) Calculations of ($\Gamma_{12}\ \Theta_2/\Gamma_{11}\ \Theta_1$) as a function of the total gas phase pressure $p_t = p_1 + p_2$. (c) Calculations of ($\Gamma_{12}\ \Theta_2/\Gamma_{11}\ \Theta_1$) as a function of the total loading Θ_t. The calculations of the elements Γ_{ij} are obtained using the simplified Equations (16) that should serve as reasonable approximations.

Figure 19. (a) Experimental data[35] on self-diffusivities of nC6 and 2-methylpentane (2MP) as a function of the loading of 2MP, keeping the total loading Θ_t = 3.5/uc. (b) Ratio of the self-diffusivity of nC6 to that of 2MP, calculated from the experimental data of Schuring et al.[35]

Figure 20. Calculations of the ratios $\frac{\Delta_{12}}{\Delta_{11}}$, and $\frac{\Delta_{21}}{\Delta_{21}}$ for nC6/2MP mixture diffusion in MFI. The parameters ($Đ_1/Đ_2$) = 100 and ($Đ_1/Đ_{12}$) =1.

Figure 21. Discretization scheme for a single spherical crystallite of MFI.

Figure 22. (a, b, c, d, e, f) Radial profiles of the loadings of nC6 and 2MP within MFI crystal, for conditions corresponding to Run 1 as specified in the legend to Figure 23, monitored at times (a) t = 1.23 s, (b) t = 5 s, (c) t = 10.2 s, (d) t = 50.6 s, and (e) t = 832 s.

Figure 23. (a) CBMC simulations of mixture loadings within the pressure range encountered in Run 1. (b) Comparison of the Maxwell-Stefan model simulation results using equation (32) with IRM experimental data for transient uptake. (c) Maxwell-Stefan model simulations using equation (37) in which the matrix of thermodynamic correction factors is assumed to be the identity matrix. Input data simulation of Run 1: $Đ_1/r_c^2$ = 0.016 s^{-1}; $Đ_2/r_c^2$ = 1.6×10^{-4} s^{-1}; $t = 0$; $p_1(r_c,0) = p_2(r_c,0)$ = 0 Pa; $t \geq 0$; $p_1(r_c,t) = p_2(r_c,t)$ = 1.3 Pa. The mixture thermodynamics equilibrium is determined using the IAST.

Figure 24. (a) CBMC simulations of mixture loadings within the pressure range encountered in Run 2. (b) Comparison of the Maxwell-Stefan model simulation results using equation (32) with IRM experimental data for transient uptake. Input data simulation of Run 2: $Đ_1/r_c^2$ = 0.02 s^{-1}; $Đ_2/r_c^2$ = 2×10^{-4} s^{-1}; $t = 0$; $p_1(r_c,0) = p_2(r_c,0)$ = 1.3 Pa; $t \geq 0$; $p_1(r_c,t) = p_2(r_c,t)$ = 2 Pa. The mixture thermodynamics equilibrium is determined using the IAST.

Figure 25. (a) CBMC simulations of mixture loadings within the pressure range encountered in Run 3. (b) Comparison of the Maxwell-Stefan model simulation results using equation (32) with IRM experimental data for transient uptake. Input data simulation of Run 3: $Đ_1/r_c^2$ = 0.04 s^{-1}; $Đ_2/r_c^2$ = 4×10^{-4} s^{-1}; $t = 0$; $p_1(r_c,0) = p_2(r_c,0)$ = 2 Pa; $t \geq 0$; $p_1(r_c,t) = p_2(r_c,t)$ = 6.1 Pa. The mixture thermodynamics equilibrium is determined using the RAST.

Figure 26. (a) CBMC simulations of mixture loadings within the pressure range encountered in Run 4. (b) Comparison of the Maxwell-Stefan model simulation results using equation (32) with IRM experimental data for transient uptake. (c) Comparison of the Maxwell-Stefan model simulation results, using Equations (20), (21), and (22), with IRM experimental data for transient uptake. Input data simulation of Run 4: $Đ_1/r_c^2$ = 0.16 s^{-1}; $Đ_2/r_c^2$ = 1.6×10^{-3} s^{-1}; $t = 0$; $p_1(r_c,0) = p_2(r_c,0)$ = 6.1 Pa; $t \geq 0$; $p_1(r_c,t) = p_2(r_c,t)$ = 51 Pa. The mixture thermodynamics equilibrium is determined using the RAST.

Figure 27.(a) CBMC mixture simulations indicating the range of pressures used in Runs 1, 2, 3, and 4. (b) Summary of comparisons of the Maxwell-Stefan model simulation results using equation (32) with IRM experimental data for transient uptake for Runs 1, 2, 3, and 4.

Figure 28. Plot of the fitted diffusivity values, $Đ_1/r_c^2$, and $Đ_2/r_c^2$ as a function of the 2MP loading at the end of the equilibration of each of the four runs.

Figure 29. Transient desorption kinetics for nC6/2MP mixture. $Đ_1/r_c^2 = 0.016$ s^{-1}; $Đ_2/r_c^2 = 1.6\times10^{-4}$ s^{-1}; $t = 0$; $p_1(r_c,0) = p_2(r_c,0) = 4$ Pa; $t \geq 0$; $p_1(r_c,t) = p_2(r_c,t) = 0.4$ Pa. The mixture thermodynamics equilibrium is determined using the IAST. The continuous solid lines using the flux equations (32), neglecting correlation effects. The dashed lines are simulations using the simplified equation (37), neglecting thermodynamic coupling.

Figure 30. Transient uptake of nC4/iC4 mixture in MFI at 298 K using the Maxwell-Stefan model with flux equations (32). Input data: $Đ_1/r_c^2 = 0.08$ s^{-1}; $Đ_2/r_c^2 = 4\times10^{-3}$ s^{-1}; $t = 0$; $p_1(r_c,0) = p_2(r_c,0) = 0$ Pa; $t \geq 0$; $p_1(r_c,t) = p_2(r_c,t) = 200$ Pa. The mixture thermodynamics equilibrium is determined using the IAST.

Figure 1

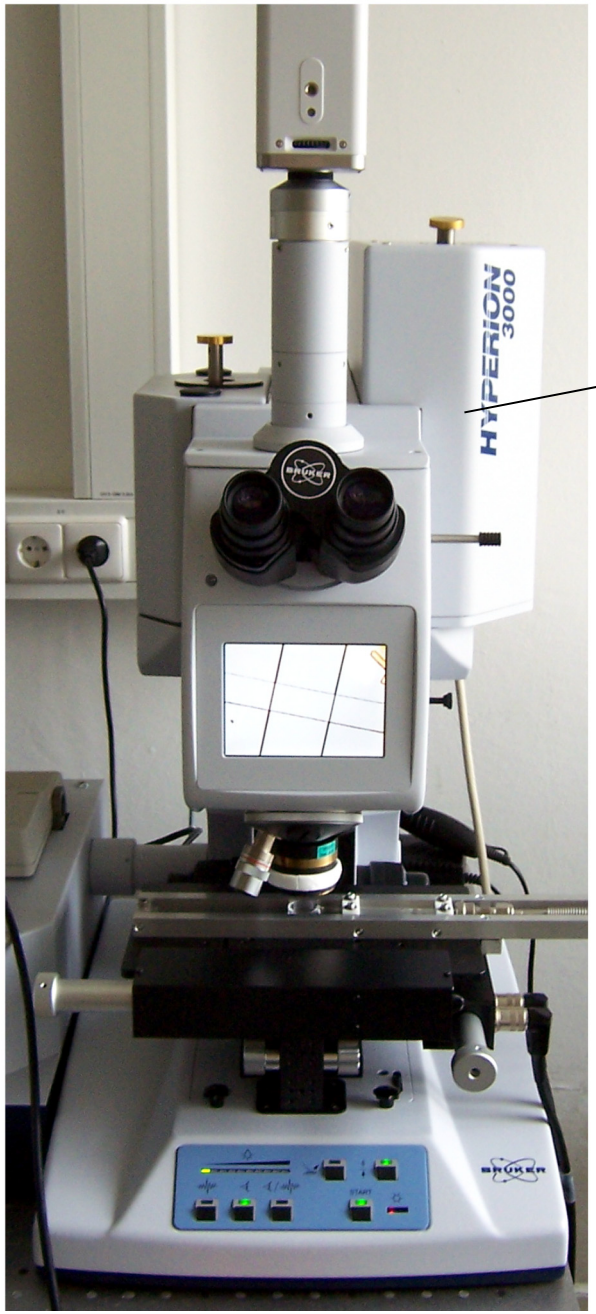

Viewing mode of microscope
for adjusting aperture

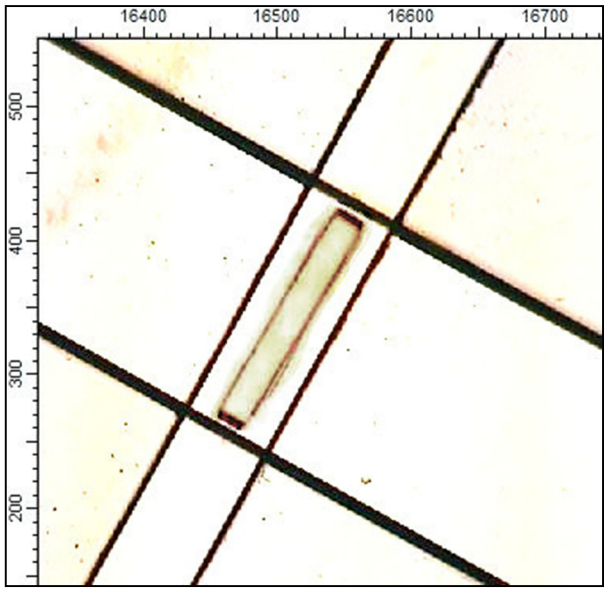

Crystal adjusted on moving platform

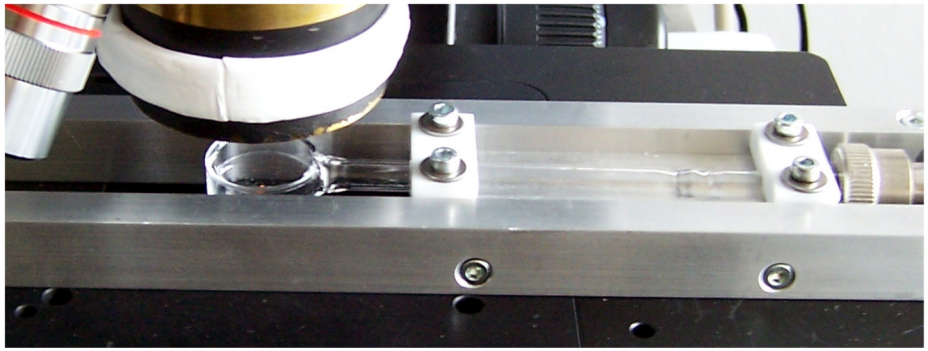

Figure 2

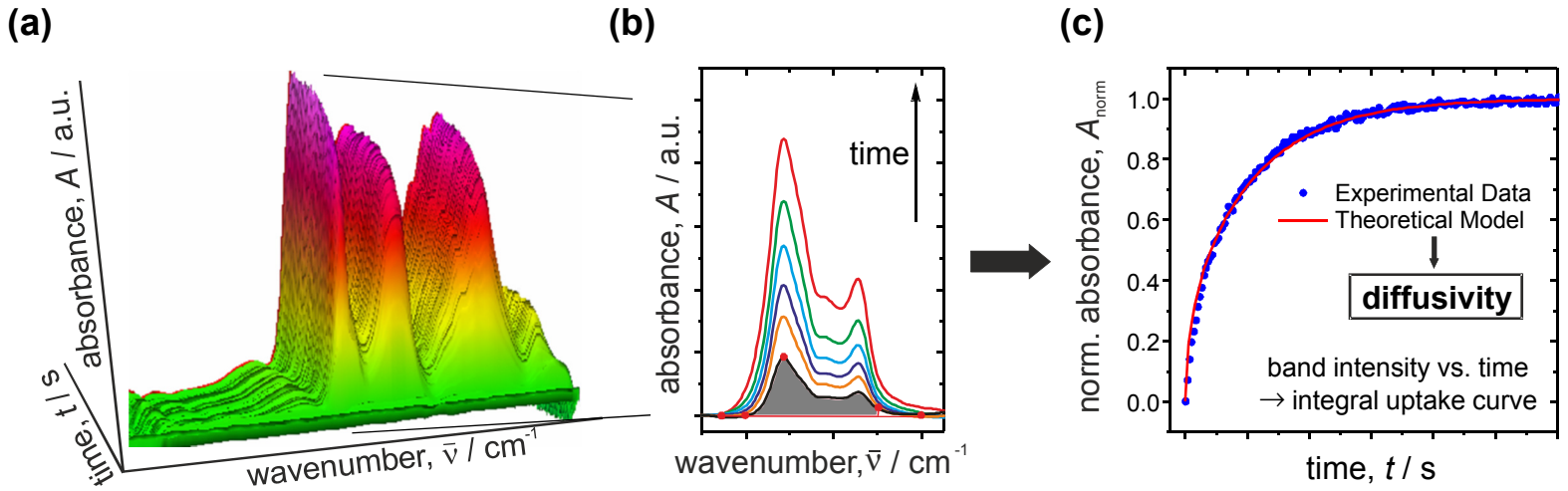
(a)
absorbance, A / a.u.
time, t / s
wavenumber, ν̄ / cm-1
(b)
absorbance, A / a.u.
time
wavenumber, ν̄ / cm-1
(c)
norm. absorbance, Anorm
1.0
0.8
0.6
0.4
0.2
0.0
Experimental Data
Theoretical Model
diffusivity
band intensity vs. time
→ integral uptake curve
time, t / s

Figure 3

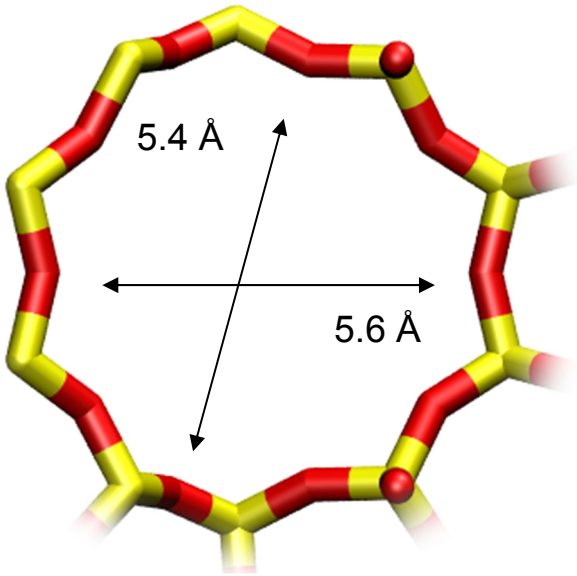

10 ring channel
of MFI viewed
along [100]

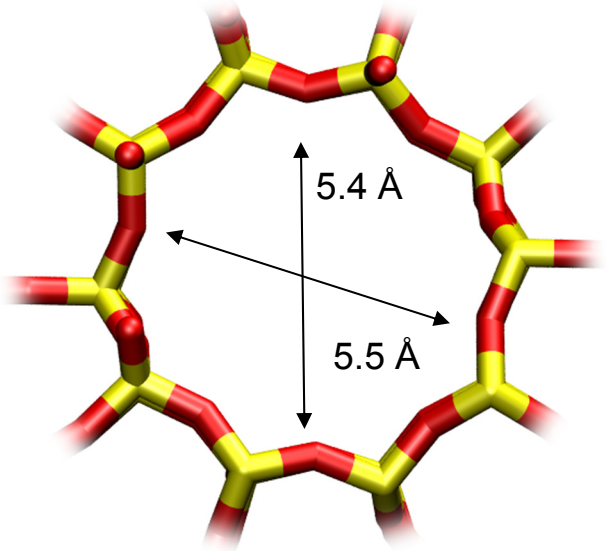

10 ring channel
of MFI viewed
along [010]

Figure 4

CBMC vs Expt data for C1, C2, and C3 in MFI

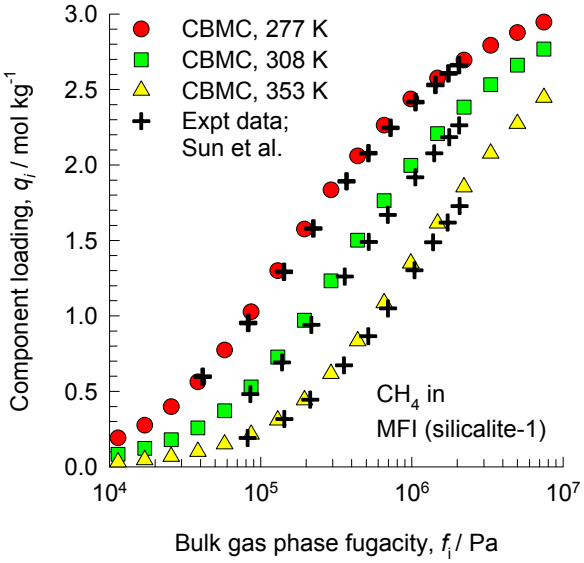

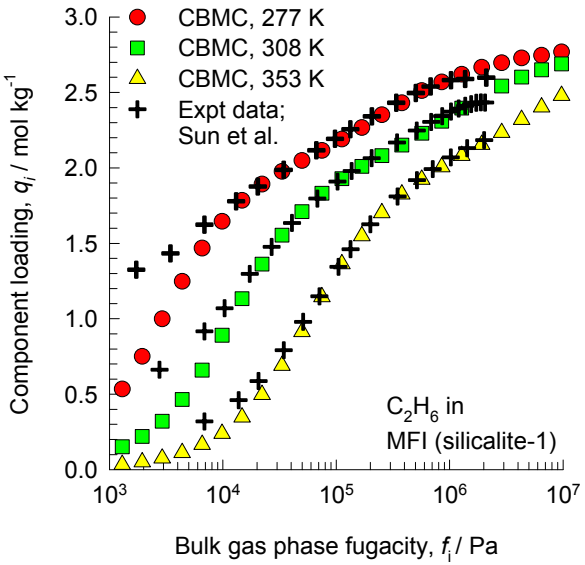

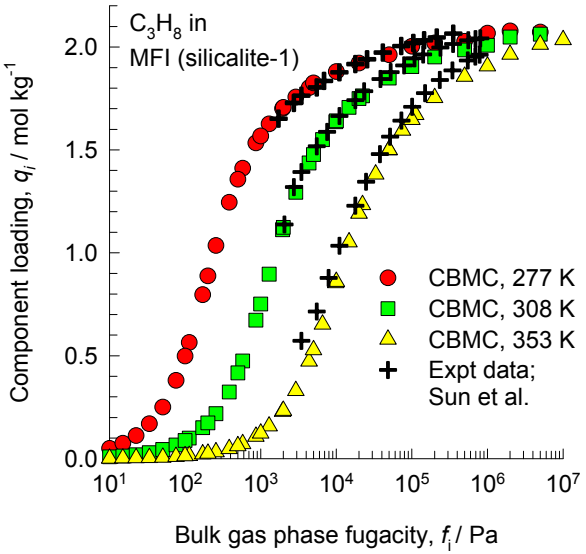

Figure 5

CBMC vs Expt data for nC4 isotherm in MFI

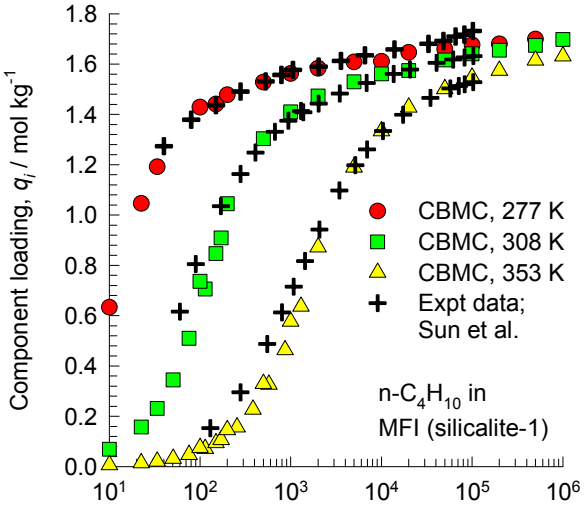

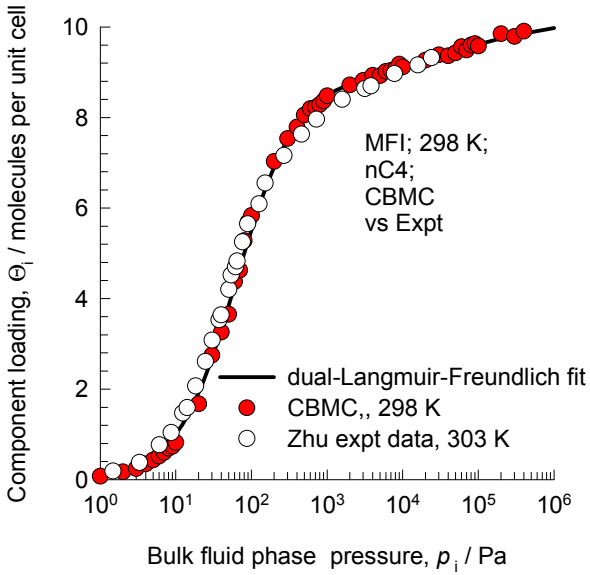

x-z view

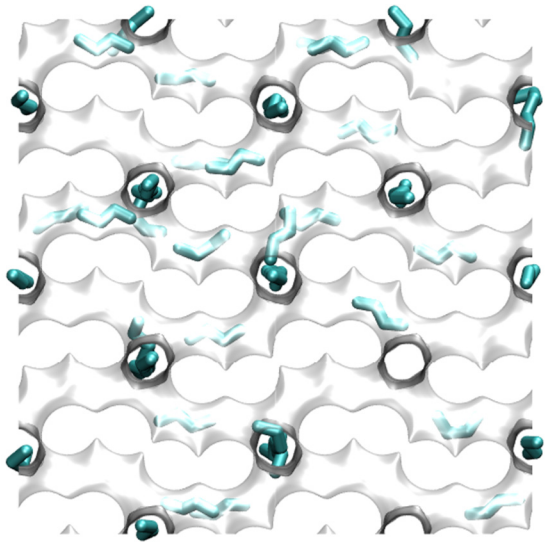

nC4 at loading of 4 molecules/uc
x-y view

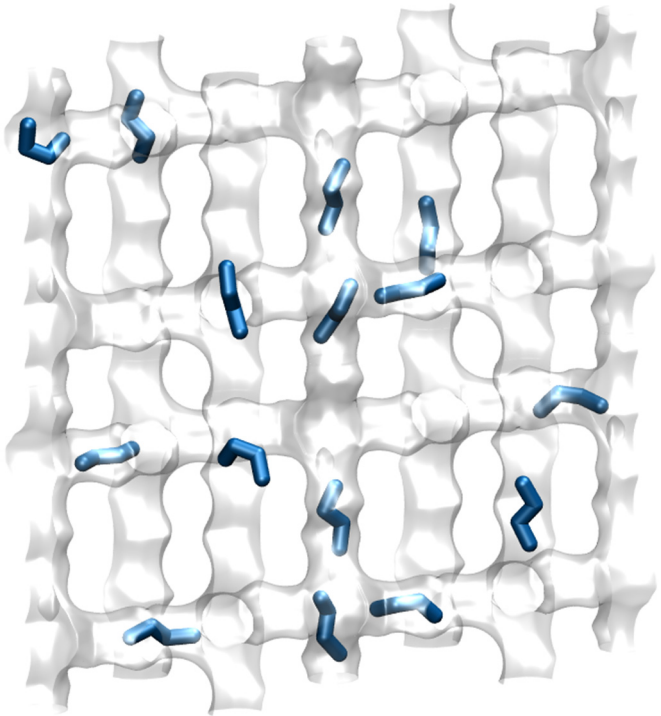

Figure 6

CBMC vs Expt data for nC6 in MFI

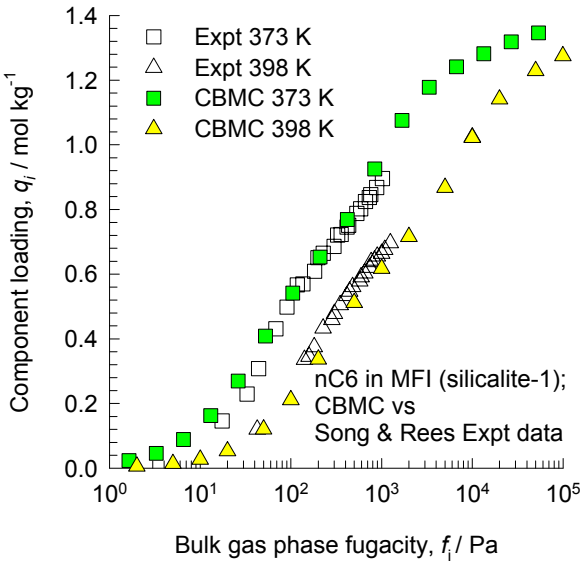

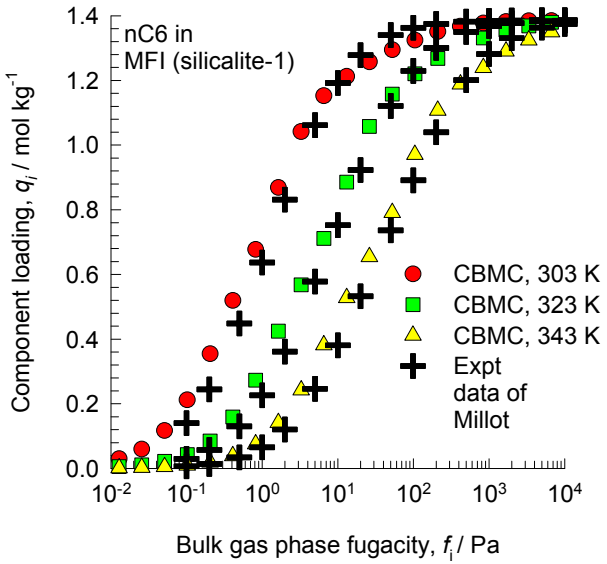

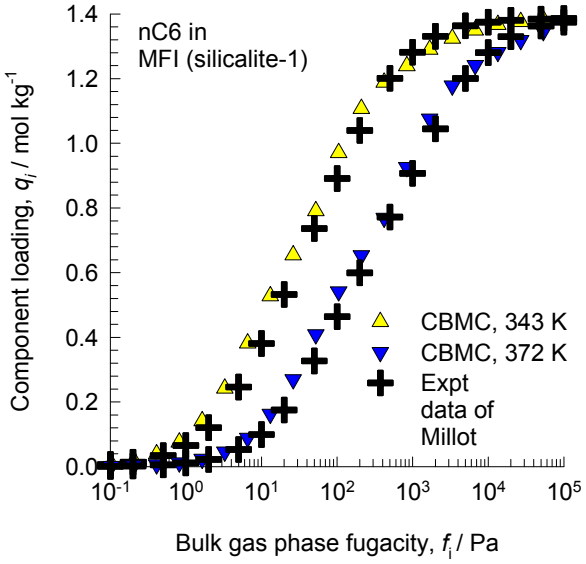

Figure 7

CBMC vs Expt data for nC7 in MFI

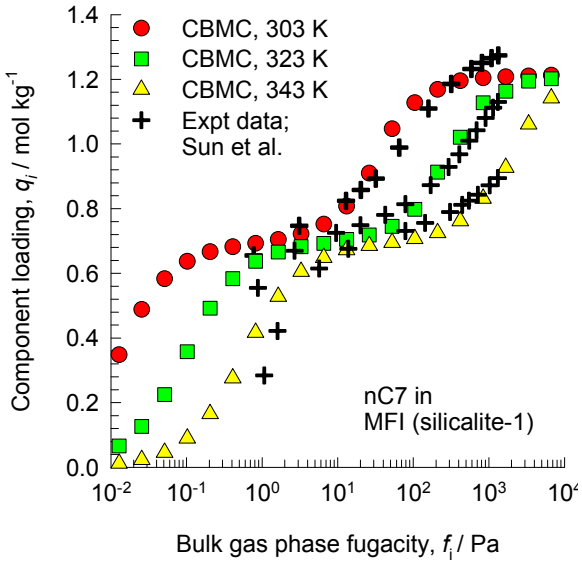

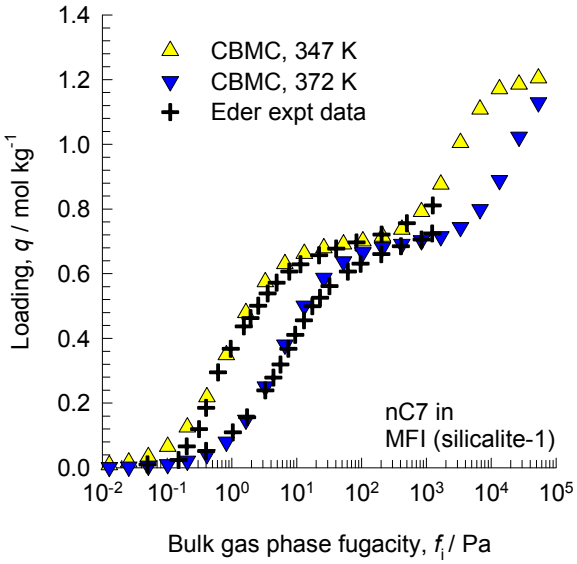

nC7 at loading of 4 molecules/uc

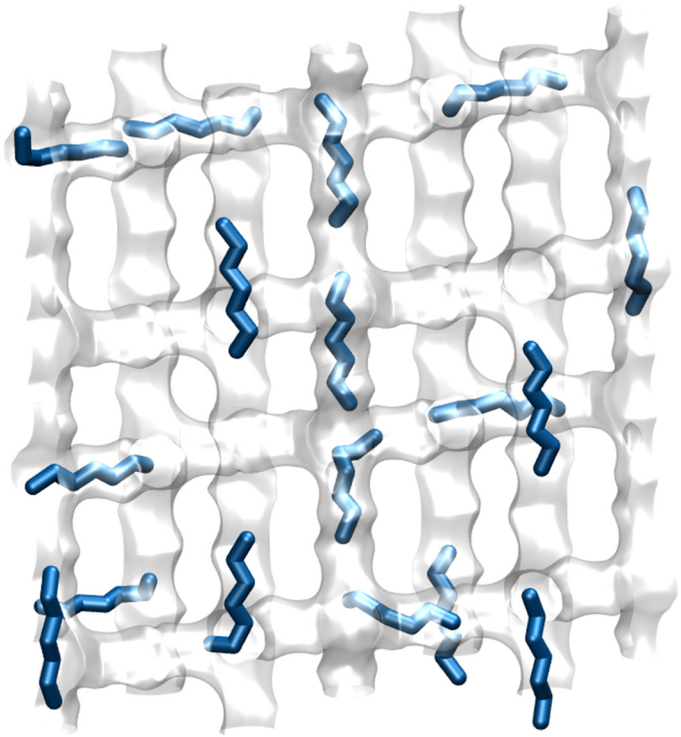

Figure 8

CBMC vs Expt data for iC4 in MFI

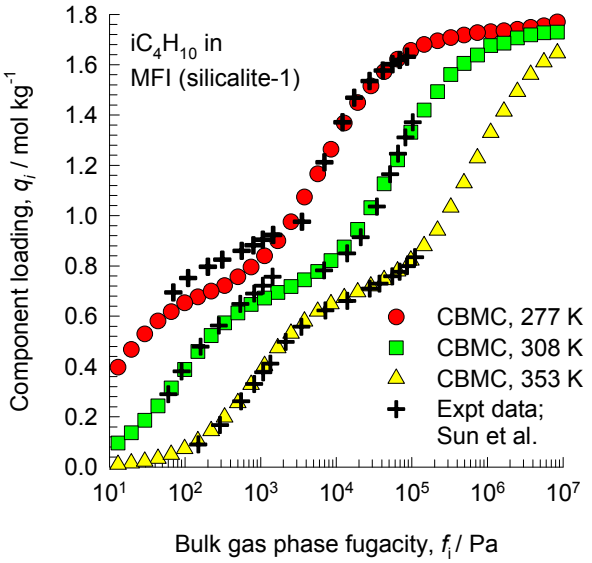

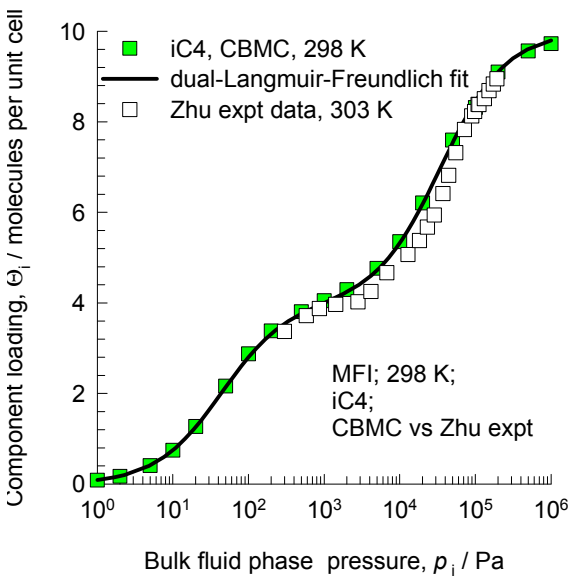

iC4 at a loading of 4/uc

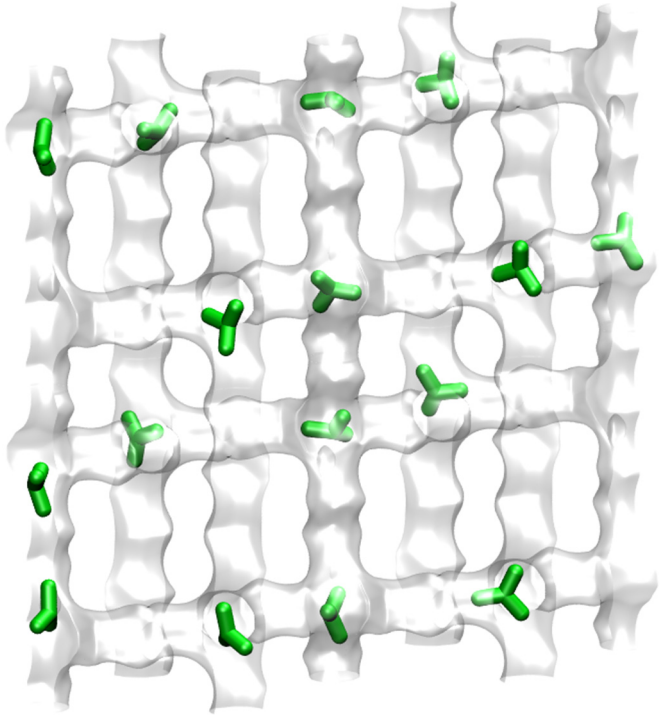

Figure 9

CBMC vs Expt data for 2MP in MFI

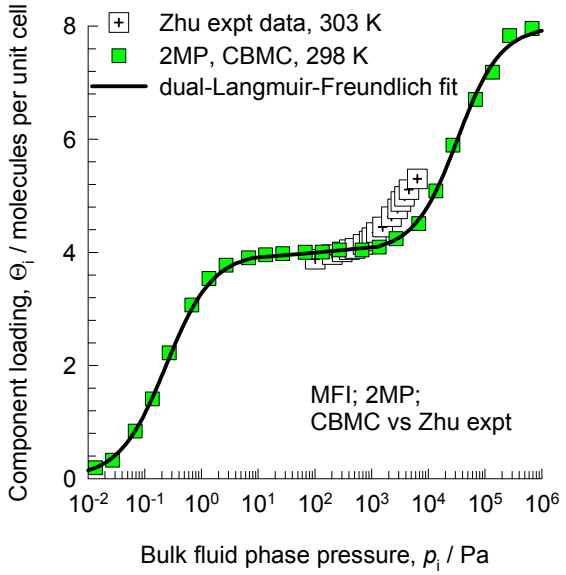

Figure 10

CBMC vs Expt data for 3MP in MFI

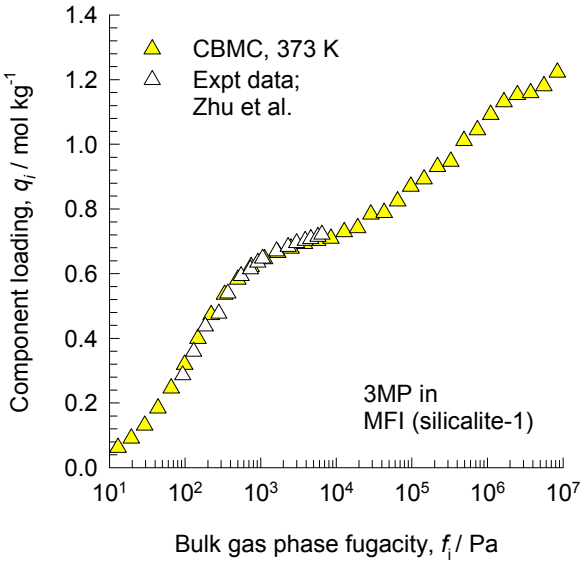

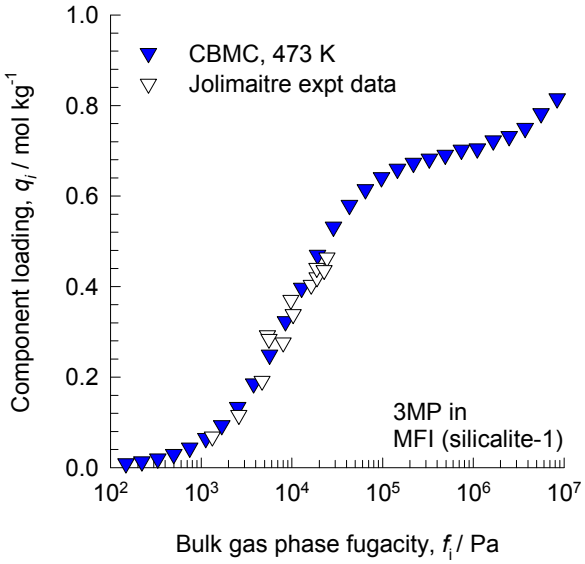

Top view of 3MP molecules

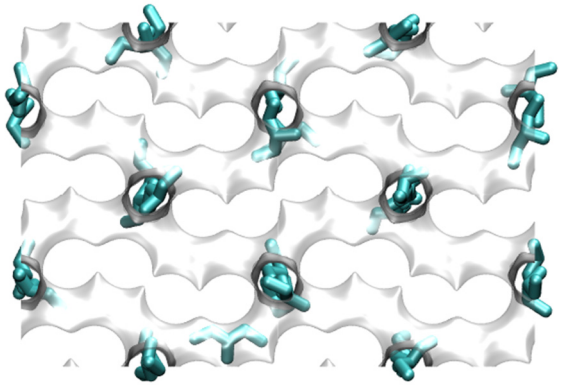

Side-on view of 3MP molecules

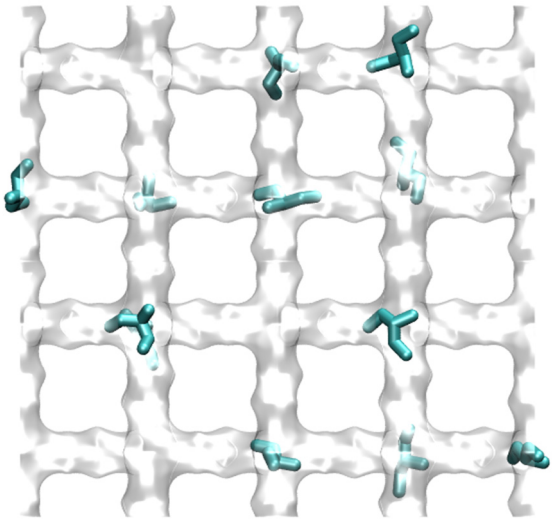

Figure 11

CBMC vs Expt data for 22DMB in MFI

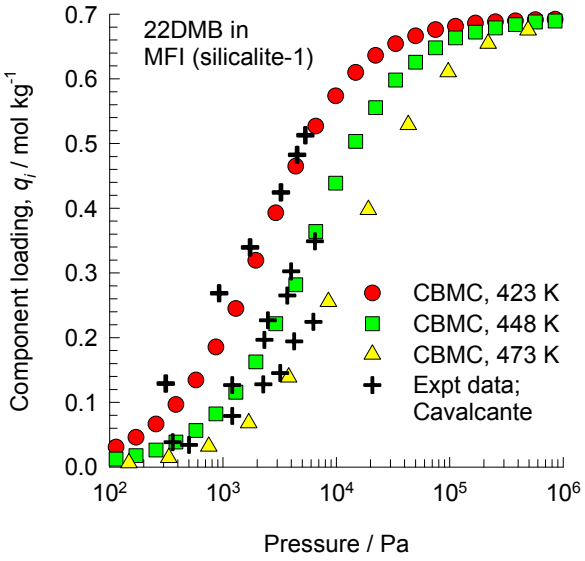

Top view of 22DMB molecules

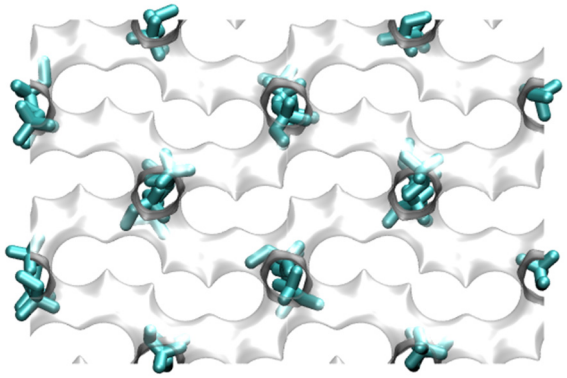

Side-on view of 22DMB molecules

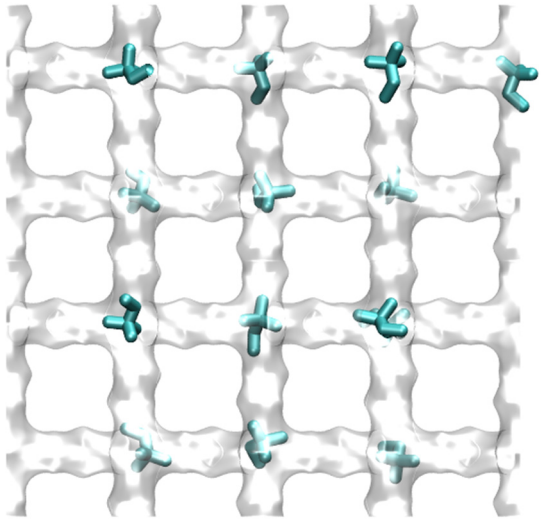

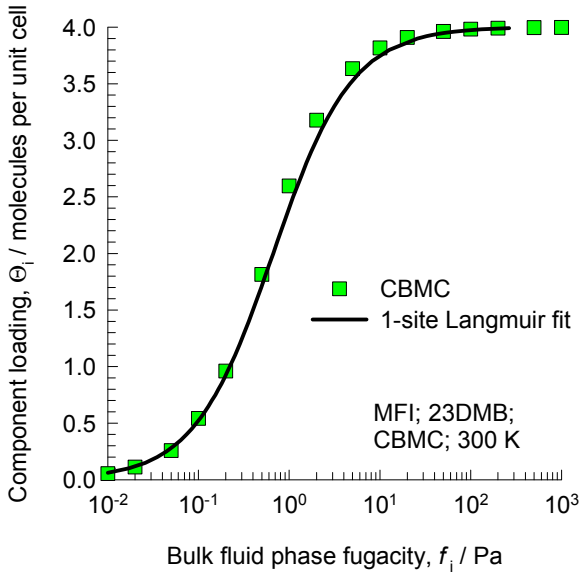

Figure 12

CBMC vs IRM for nC6 isotherm in MFI

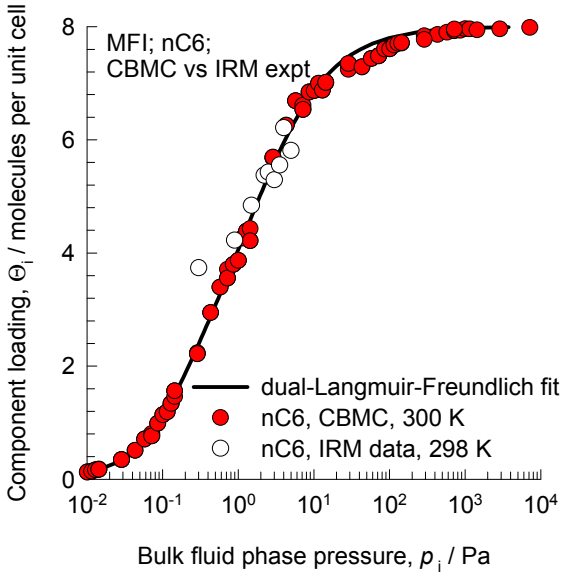

nC6 x-z view

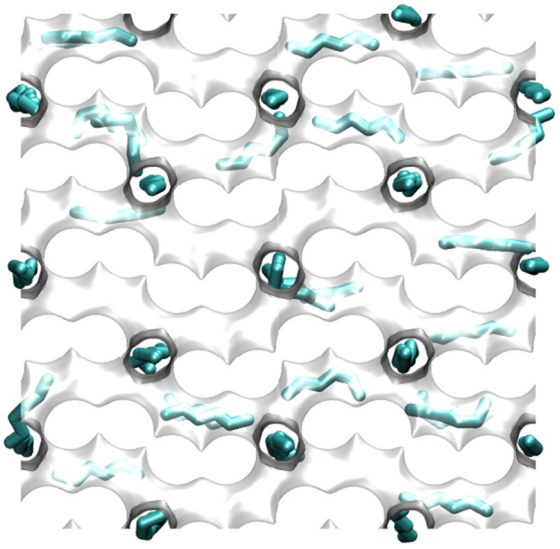

nC6 at loading of 4 molecules/uc
x-y view

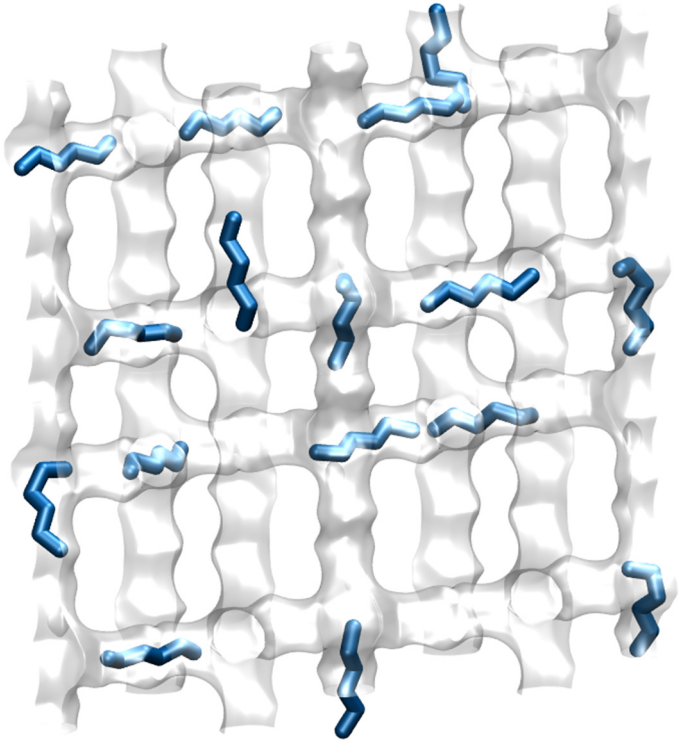

Figure 13

CBMC vs IRM for 2MP in MFI

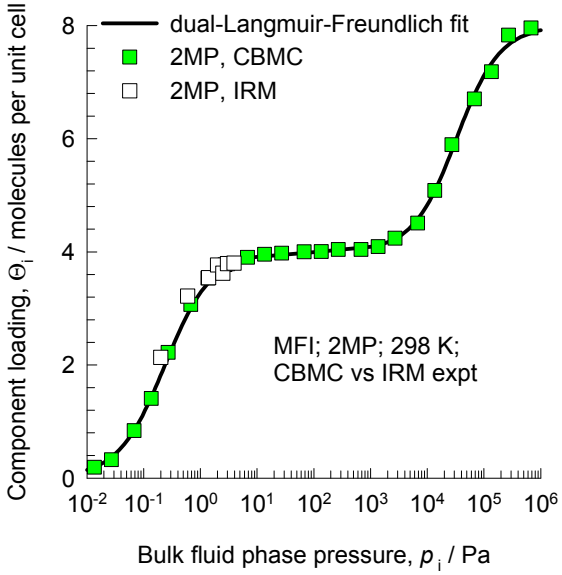

x-z view of 2MP molecules

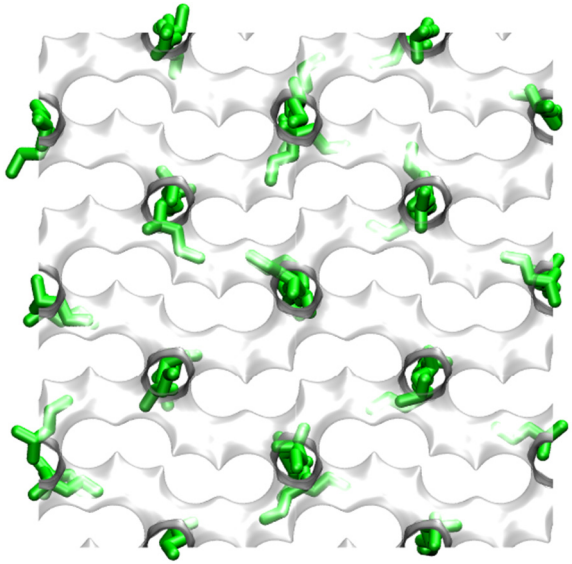

x-y view of 2MP molecules

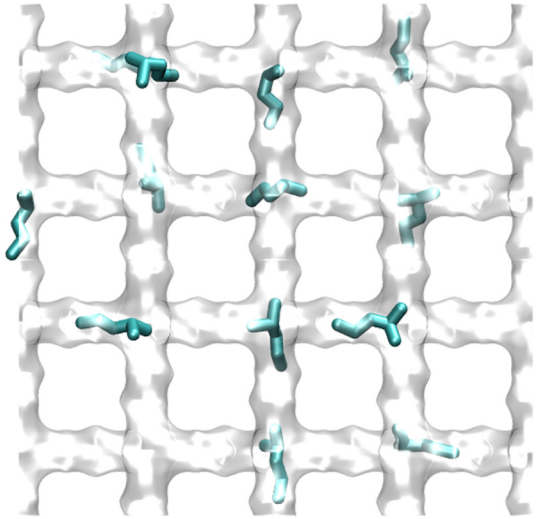

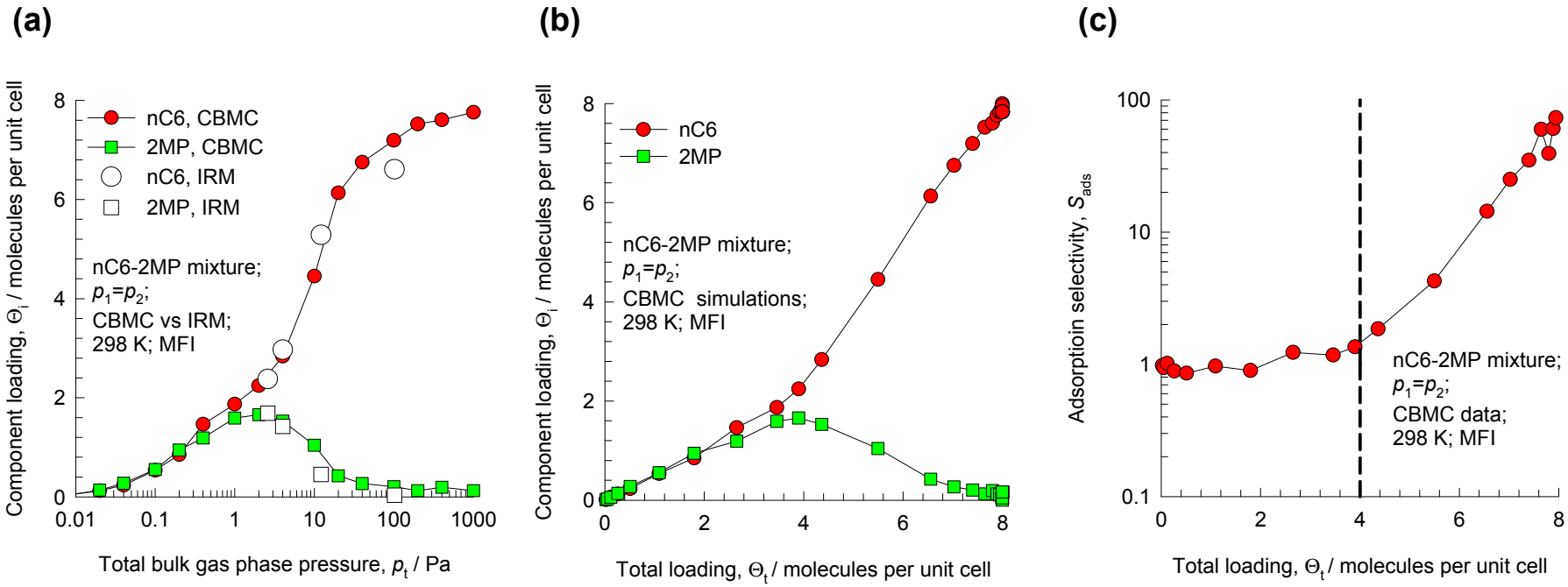
(a)
(b)
(c)
nC6, CBMC
2MP, CBMC
nC6, IRM
2MP, IRM
nC6-2MP mixture;
p_1=p_2;
CBMC vs IRM;
298 K; MFI
Component loading, Θ_i / molecules per unit cell
Total bulk gas phase pressure, p_t / Pa
nC6
2MP
nC6-2MP mixture;
p_1=p_2;
CBMC simulations;
298 K; MFI
Total loading, Θ_t / molecules per unit cell
Adsorptioin selectivity, S_{ads}
nC6-2MP mixture;
p_1=p_2;
CBMC data;
298 K; MFI
Total loading, Θ_t / molecules per unit cell

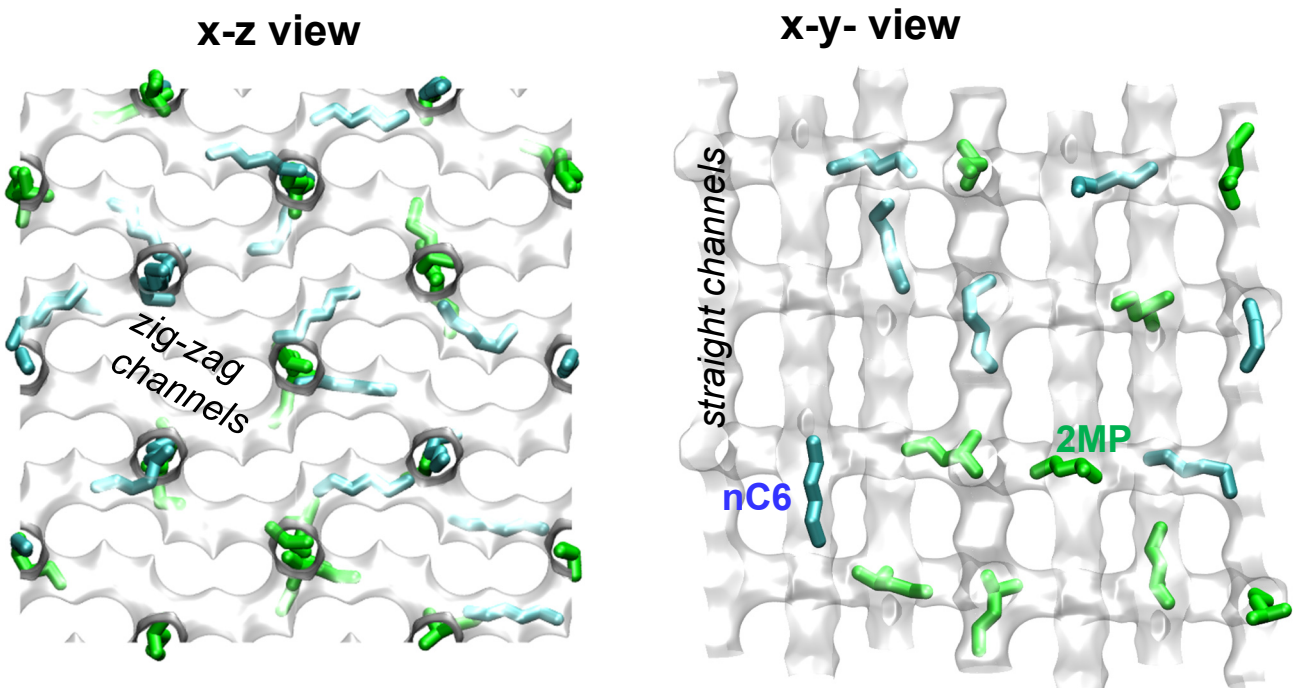
x-z view
zig-zag channels
x-y- view
straight channels
2MP
nC6

Figure 15

(a)

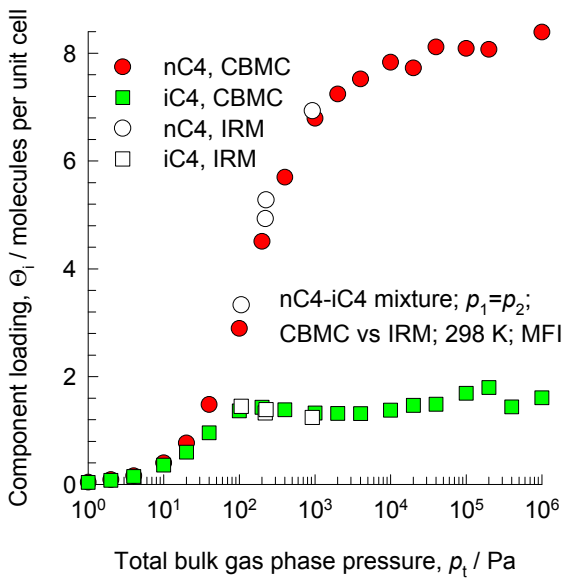

(b)

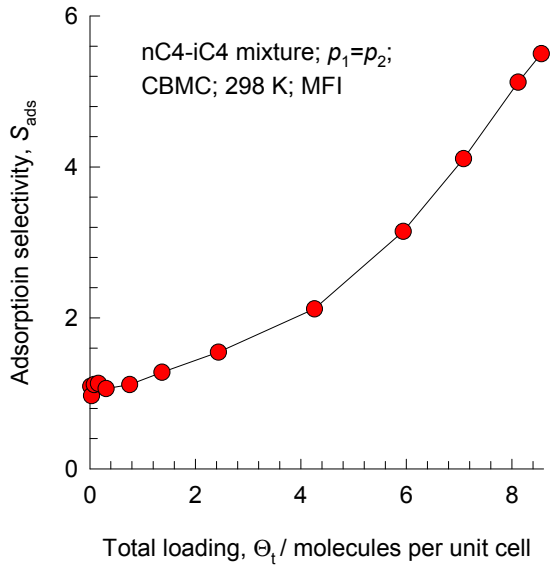

x-z view

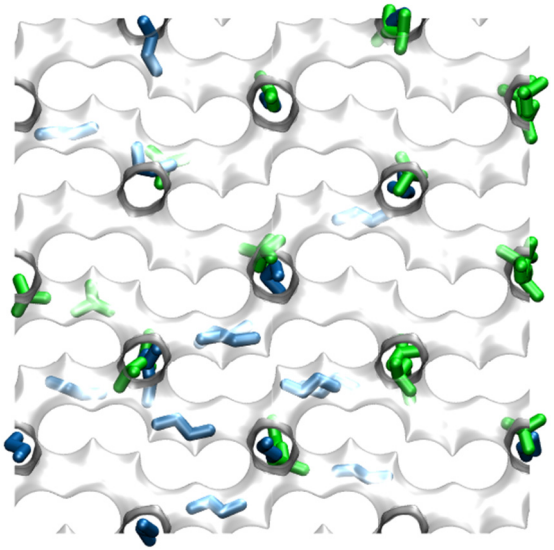

x-y view

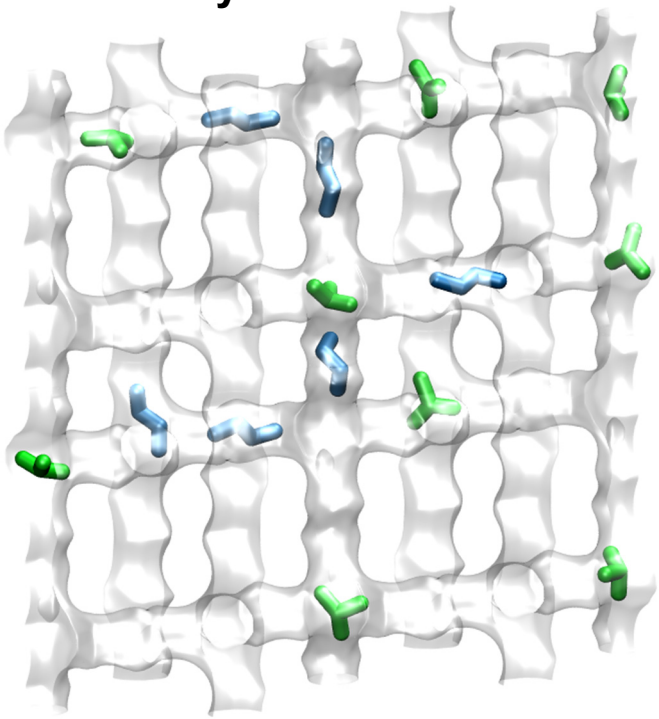

Figure 16

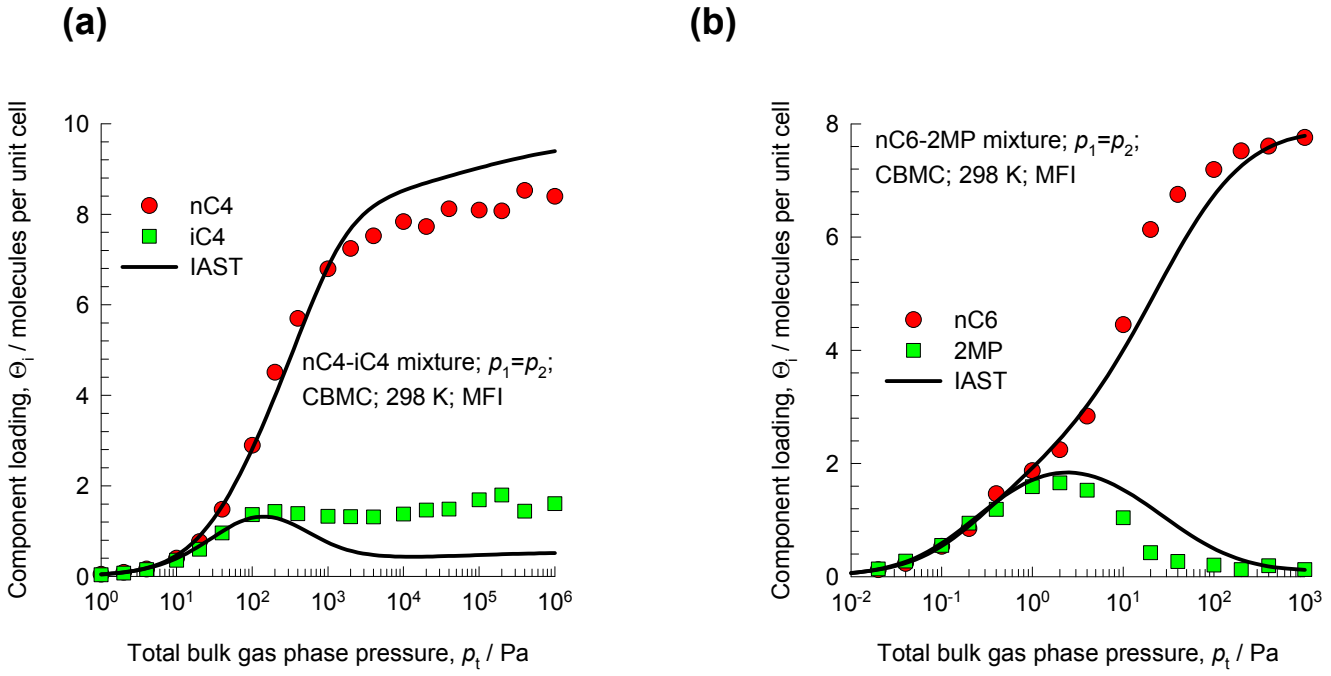
(a)
(b)
Component loading, Θ_i / molecules per unit cell
nC4
iC4
IAST
nC4-iC4 mixture; $p_1=p_2$;
CBMC; 298 K; MFI
Total bulk gas phase pressure, p_t / Pa
nC6-2MP mixture; $p_1=p_2$;
CBMC; 298 K; MFI
nC6
2MP
IAST
Total bulk gas phase pressure, p_t / Pa

Figure 17

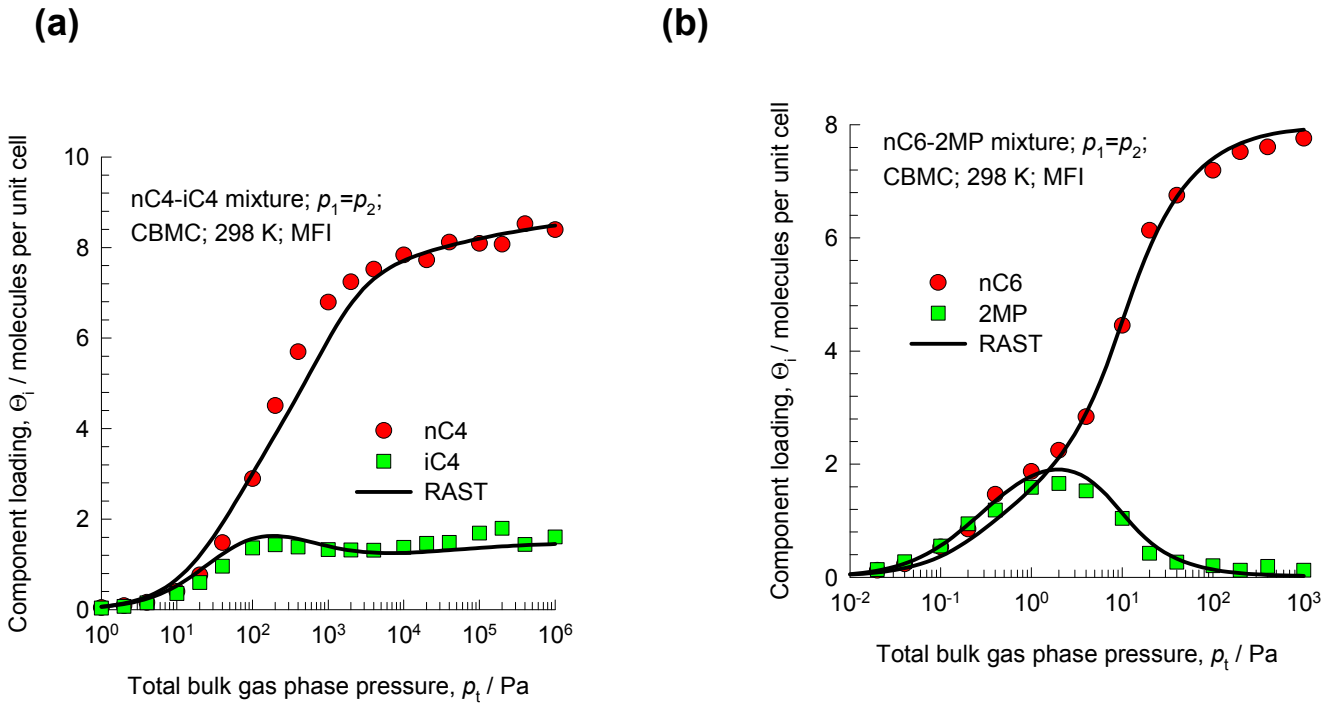
(a)
nC4-iC4 mixture; p_1=p_2;
CBMC; 298 K; MFI
nC4
iC4
RAST
Component loading, Θ_i / molecules per unit cell
Total bulk gas phase pressure, p_t / Pa
(b)
nC6-2MP mixture; p_1=p_2;
CBMC; 298 K; MFI
nC6
2MP
RAST
Component loading, Θ_i / molecules per unit cell
Total bulk gas phase pressure, p_t / Pa

Figure 18

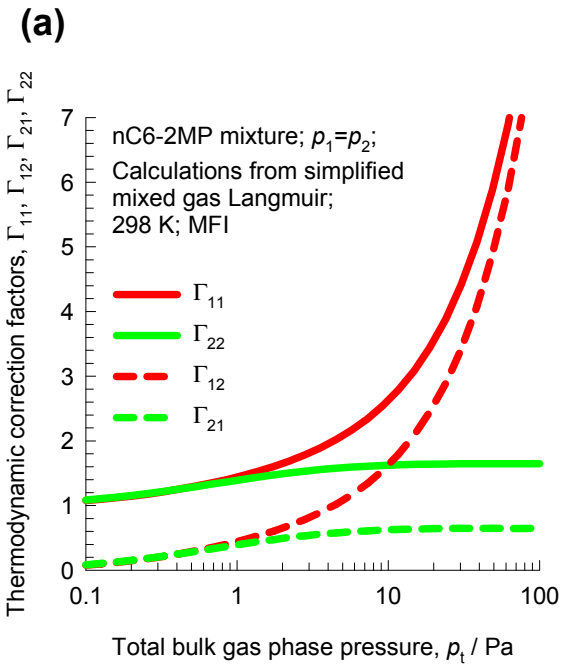
(a)
Thermodynamic correction factors, Γ_{11}, Γ_{12}, Γ_{21}, Γ_{22}
nC6-2MP mixture; $p_1=p_2$;
Calculations from simplified
mixed gas Langmuir;
298 K; MFI
Γ_{11}
Γ_{22}
Γ_{12}
Γ_{21}
0
1
2
3
4
5
6
7
0.1
1
10
100
Total bulk gas phase pressure, p_t / Pa

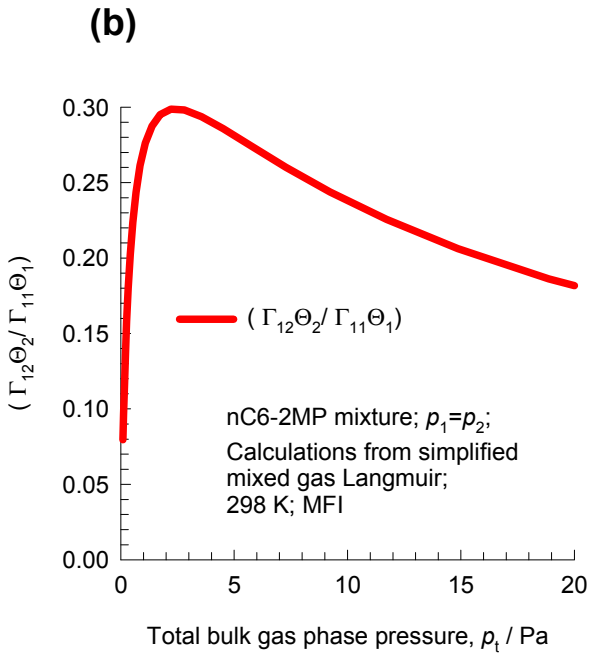
(b)
$(\Gamma_{12}\Theta_2/\Gamma_{11}\Theta_1)$
$(\Gamma_{12}\Theta_2/\Gamma_{11}\Theta_1)$
nC6-2MP mixture; $p_1=p_2$;
Calculations from simplified
mixed gas Langmuir;
298 K; MFI
0.00
0.05
0.10
0.15
0.20
0.25
0.30
0
5
10
15
20
Total bulk gas phase pressure, p_t / Pa

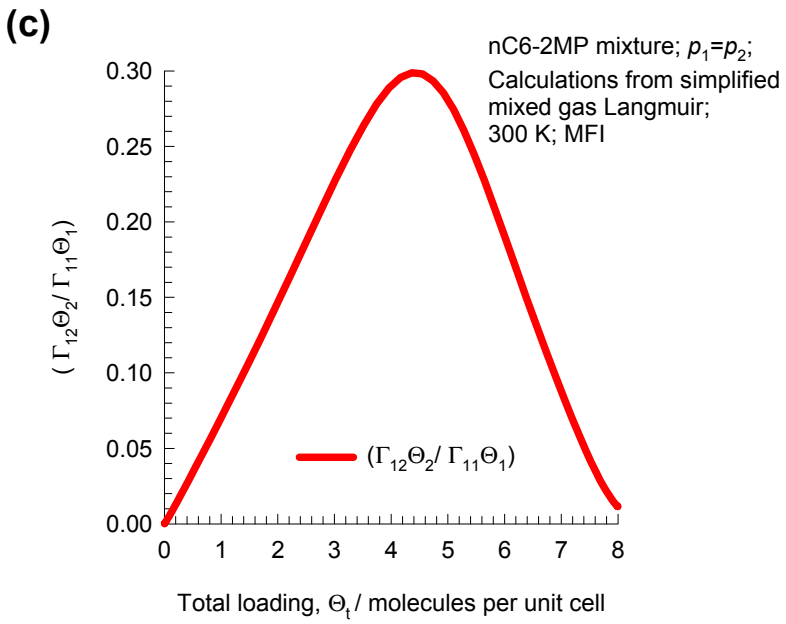
(c)
nC6-2MP mixture; $p_1=p_2$;
Calculations from simplified
mixed gas Langmuir;
300 K; MFI
$(\Gamma_{12}\Theta_2/\Gamma_{11}\Theta_1)$
$(\Gamma_{12}\Theta_2/\Gamma_{11}\Theta_1)$
0.00
0.05
0.10
0.15
0.20
0.25
0.30
0
1
2
3
4
5
6
7
8
Total loading, Θ_t / molecules per unit cell

Figure 19

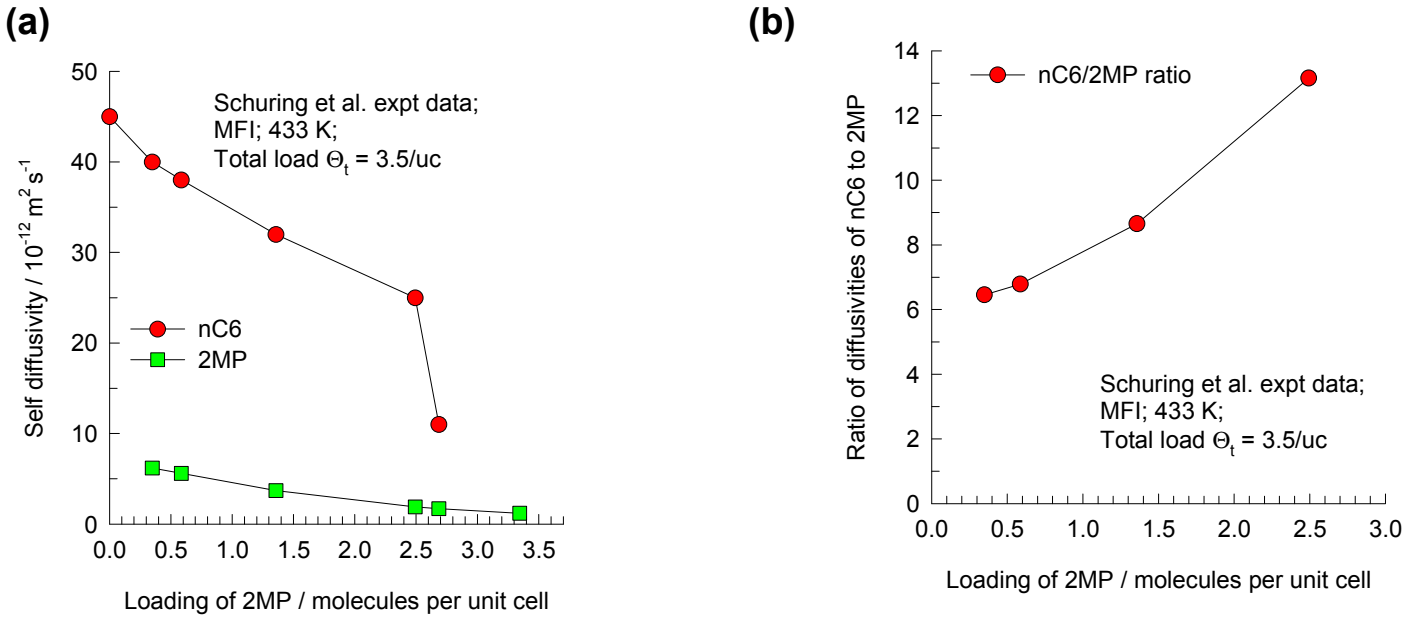
(a)
Schuring et al. expt data;
MFI; 433 K;
Total load Θt = 3.5/uc
nC6
2MP
Self diffusivity / 10-12 m2 s-1
Loading of 2MP / molecules per unit cell
(b)
nC6/2MP ratio
Ratio of diffusivities of nC6 to 2MP
Schuring et al. expt data;
MFI; 433 K;
Total load Θt = 3.5/uc
Loading of 2MP / molecules per unit cell

Figure 20

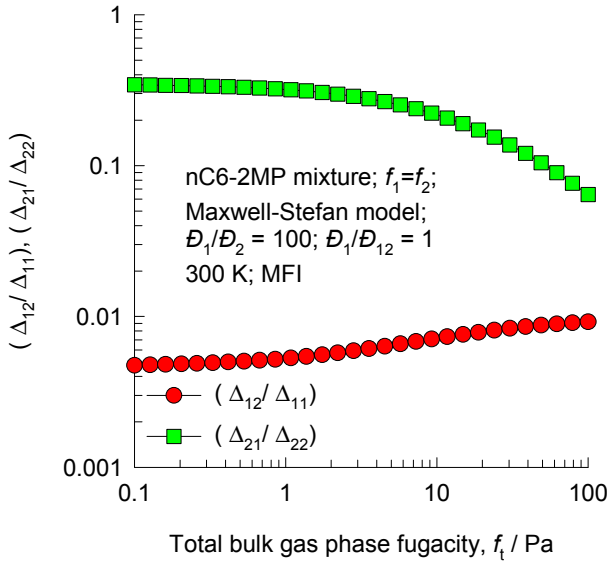
1
0.1
0.01
0.001
0.1
1
10
100
(Δ12/ Δ11), (Δ21/ Δ22)
Total bulk gas phase fugacity, ft / Pa
nC6-2MP mixture; f1=f2;
Maxwell-Stefan model;
Đ1/Đ2 = 100; Đ1/Đ12 = 1
300 K; MFI
(Δ12/ Δ11)
(Δ21/ Δ22)

Figure 21

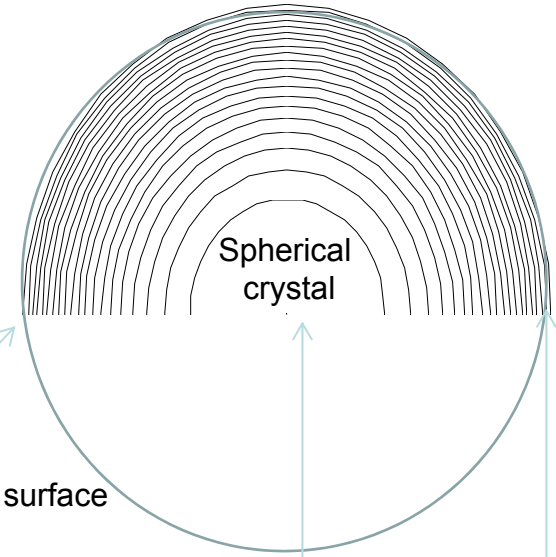

The component loadings at surface of crystal at $q_i(r_c,t)$ is in thermodynamic equilibrium with the surrounding bulk gas mixture that does not vary with time. The equilibrium loadings are determined from IAST or RAST, as appropriate.

Figure 22

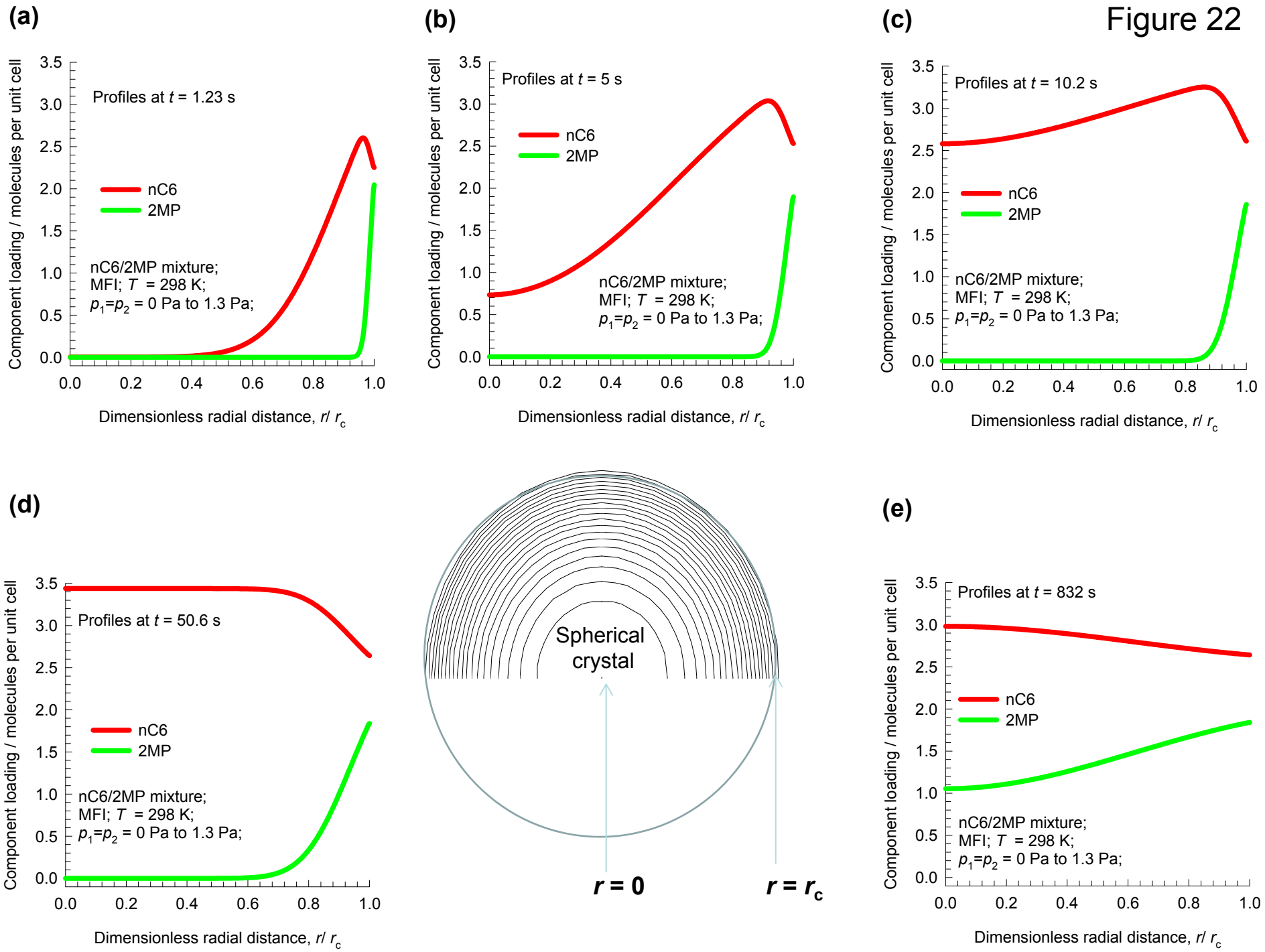
(a)
Profiles at t = 1.23 s
nC6
2MP
nC6/2MP mixture;
MFI; T = 298 K;
p1=p2 = 0 Pa to 1.3 Pa;
Component loading / molecules per unit cell
Dimensionless radial distance, r/ rc
(b)
Profiles at t = 5 s
nC6
2MP
nC6/2MP mixture;
MFI; T = 298 K;
p1=p2 = 0 Pa to 1.3 Pa;
Component loading / molecules per unit cell
Dimensionless radial distance, r/ rc
(c)
Profiles at t = 10.2 s
nC6
2MP
nC6/2MP mixture;
MFI; T = 298 K;
p1=p2 = 0 Pa to 1.3 Pa;
Component loading / molecules per unit cell
Dimensionless radial distance, r/ rc
(d)
Profiles at t = 50.6 s
nC6
2MP
nC6/2MP mixture;
MFI; T = 298 K;
p1=p2 = 0 Pa to 1.3 Pa;
Component loading / molecules per unit cell
Dimensionless radial distance, r/ rc
Spherical crystal
r = 0
r = rc
(e)
Profiles at t = 832 s
nC6
2MP
nC6/2MP mixture;
MFI; T = 298 K;
p1=p2 = 0 Pa to 1.3 Pa;
Component loading / molecules per unit cell
Dimensionless radial distance, r/ rc

Figure 23

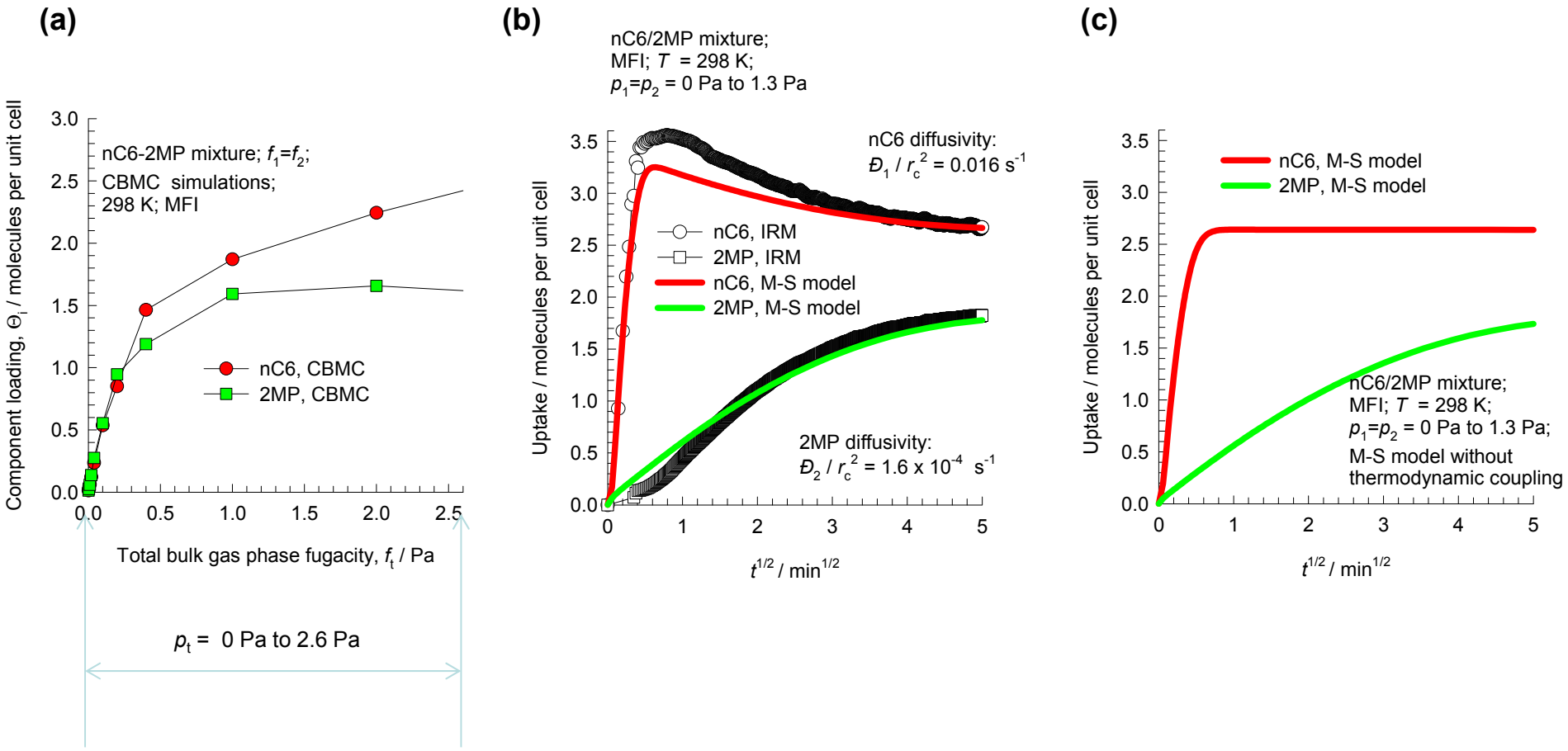
(a)
nC6-2MP mixture; f_1=f_2;
CBMC simulations;
298 K; MFI
nC6, CBMC
2MP, CBMC
Component loading, Θ_i / molecules per unit cell
Total bulk gas phase fugacity, f_t / Pa
p_t = 0 Pa to 2.6 Pa
(b)
nC6/2MP mixture;
MFI; T = 298 K;
p_1=p_2 = 0 Pa to 1.3 Pa
nC6 diffusivity:
$Đ_1 / r_c^2$ = 0.016 s^{-1}
nC6, IRM
2MP, IRM
nC6, M-S model
2MP, M-S model
2MP diffusivity:
$Đ_2 / r_c^2$ = 1.6 x 10^{-4} s^{-1}
Uptake / molecules per unit cell
$t^{1/2}$ / $min^{1/2}$
(c)
nC6, M-S model
2MP, M-S model
nC6/2MP mixture;
MFI; T = 298 K;
p_1=p_2 = 0 Pa to 1.3 Pa;
M-S model without
thermodynamic coupling
Uptake / molecules per unit cell
$t^{1/2}$ / $min^{1/2}$

Figure 24

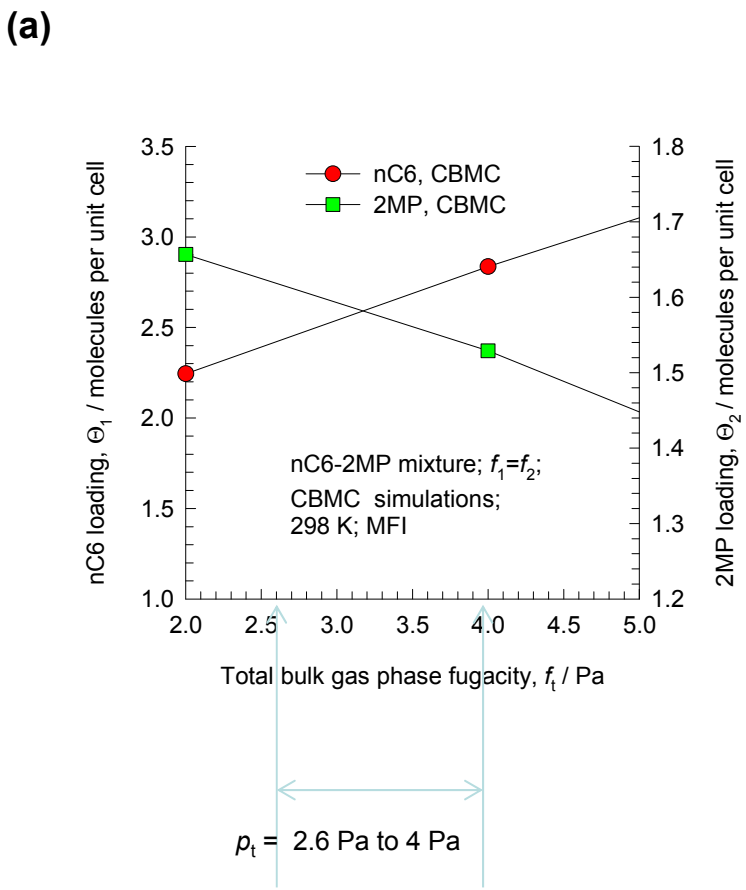
(a)
nC6, CBMC
2MP, CBMC
nC6-2MP mixture; f_1=f_2;
CBMC simulations;
298 K; MFI
nC6 loading, Θ_1 / molecules per unit cell
2MP loading, Θ_2 / molecules per unit cell
Total bulk gas phase fugacity, f_t / Pa
p_t = 2.6 Pa to 4 Pa

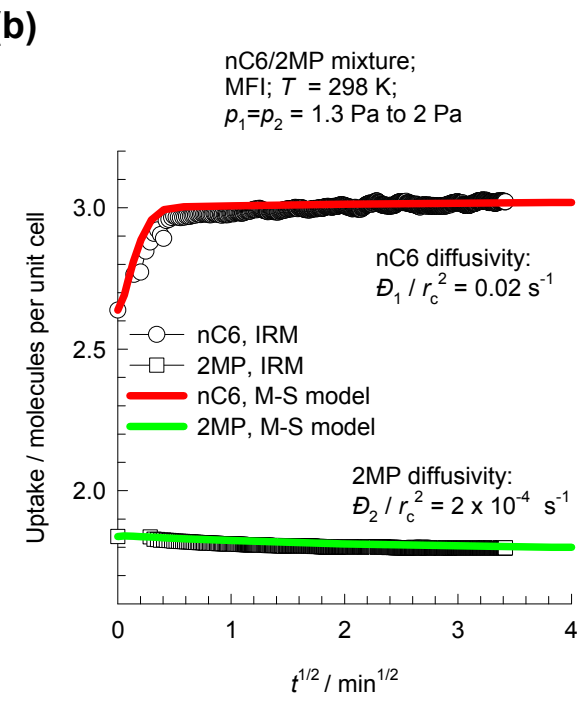
(b)
nC6/2MP mixture;
MFI; T = 298 K;
p_1=p_2 = 1.3 Pa to 2 Pa
nC6 diffusivity:
$Đ_1 / r_c^2$ = 0.02 s^{-1}
nC6, IRM
2MP, IRM
nC6, M-S model
2MP, M-S model
2MP diffusivity:
$Đ_2 / r_c^2$ = 2 x 10^{-4} s^{-1}
Uptake / molecules per unit cell
$t^{1/2}$ / $min^{1/2}$

Figure 25

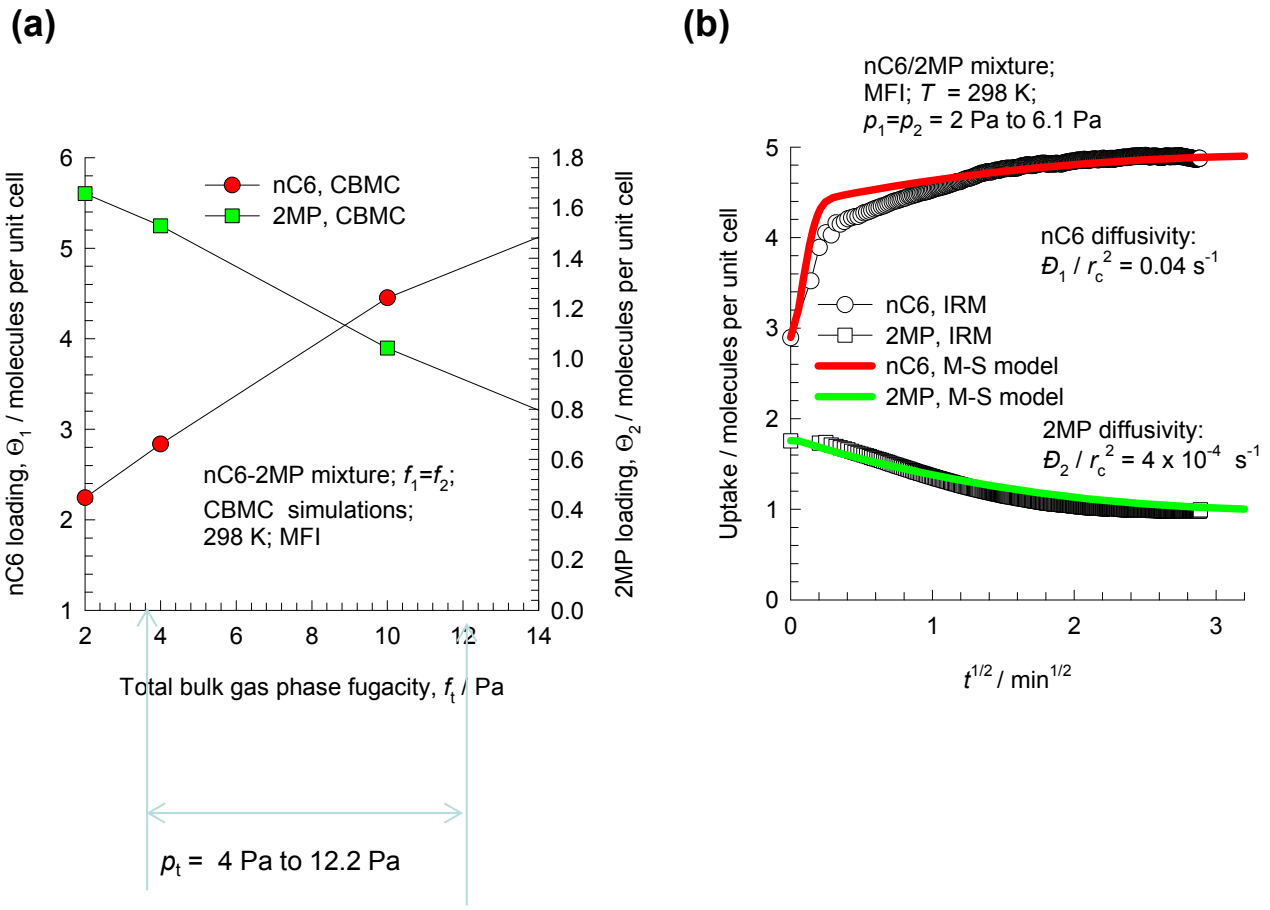
(a)
nC6, CBMC
2MP, CBMC
nC6-2MP mixture; f_1=f_2;
CBMC simulations;
298 K; MFI
nC6 loading, Θ_1 / molecules per unit cell
2MP loading, Θ_2 / molecules per unit cell
Total bulk gas phase fugacity, f_t / Pa
p_t = 4 Pa to 12.2 Pa
(b)
nC6/2MP mixture;
MFI; T = 298 K;
p_1=p_2 = 2 Pa to 6.1 Pa
nC6 diffusivity:
$Đ_1 / r_c^2$ = 0.04 s^{-1}
nC6, IRM
2MP, IRM
nC6, M-S model
2MP, M-S model
2MP diffusivity:
$Đ_2 / r_c^2$ = 4 x 10^{-4} s^{-1}
Uptake / molecules per unit cell
$t^{1/2}$ / $min^{1/2}$

Figure 26

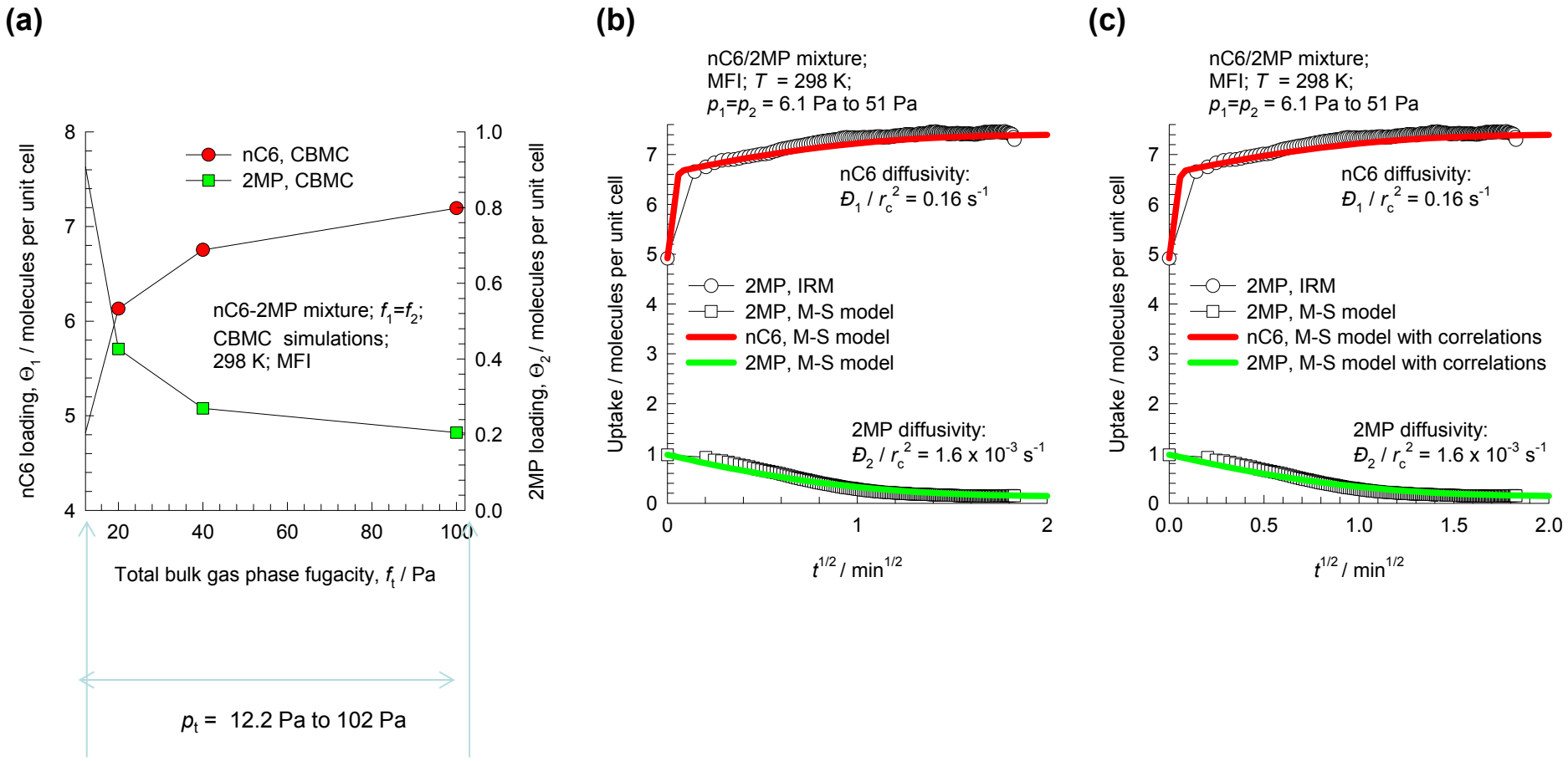
(a)
nC6, CBMC
2MP, CBMC
nC6-2MP mixture; f_1=f_2;
CBMC simulations;
298 K; MFI
nC6 loading, Θ_1 / molecules per unit cell
2MP loading, Θ_2 / molecules per unit cell
Total bulk gas phase fugacity, f_t / Pa
p_t = 12.2 Pa to 102 Pa
(b)
nC6/2MP mixture;
MFI; T = 298 K;
p_1=p_2 = 6.1 Pa to 51 Pa
nC6 diffusivity:
$Đ_1 / r_c^2$ = 0.16 s^{-1}
2MP, IRM
2MP, M-S model
nC6, M-S model
2MP, M-S model
2MP diffusivity:
$Đ_2 / r_c^2$ = 1.6 x 10^{-3} s^{-1}
Uptake / molecules per unit cell
$t^{1/2}$ / $min^{1/2}$
(c)
nC6/2MP mixture;
MFI; T = 298 K;
p_1=p_2 = 6.1 Pa to 51 Pa
nC6 diffusivity:
$Đ_1 / r_c^2$ = 0.16 s^{-1}
2MP, IRM
2MP, M-S model
nC6, M-S model with correlations
2MP, M-S model with correlations
2MP diffusivity:
$Đ_2 / r_c^2$ = 1.6 x 10^{-3} s^{-1}
Uptake / molecules per unit cell
$t^{1/2}$ / $min^{1/2}$

Figure 27

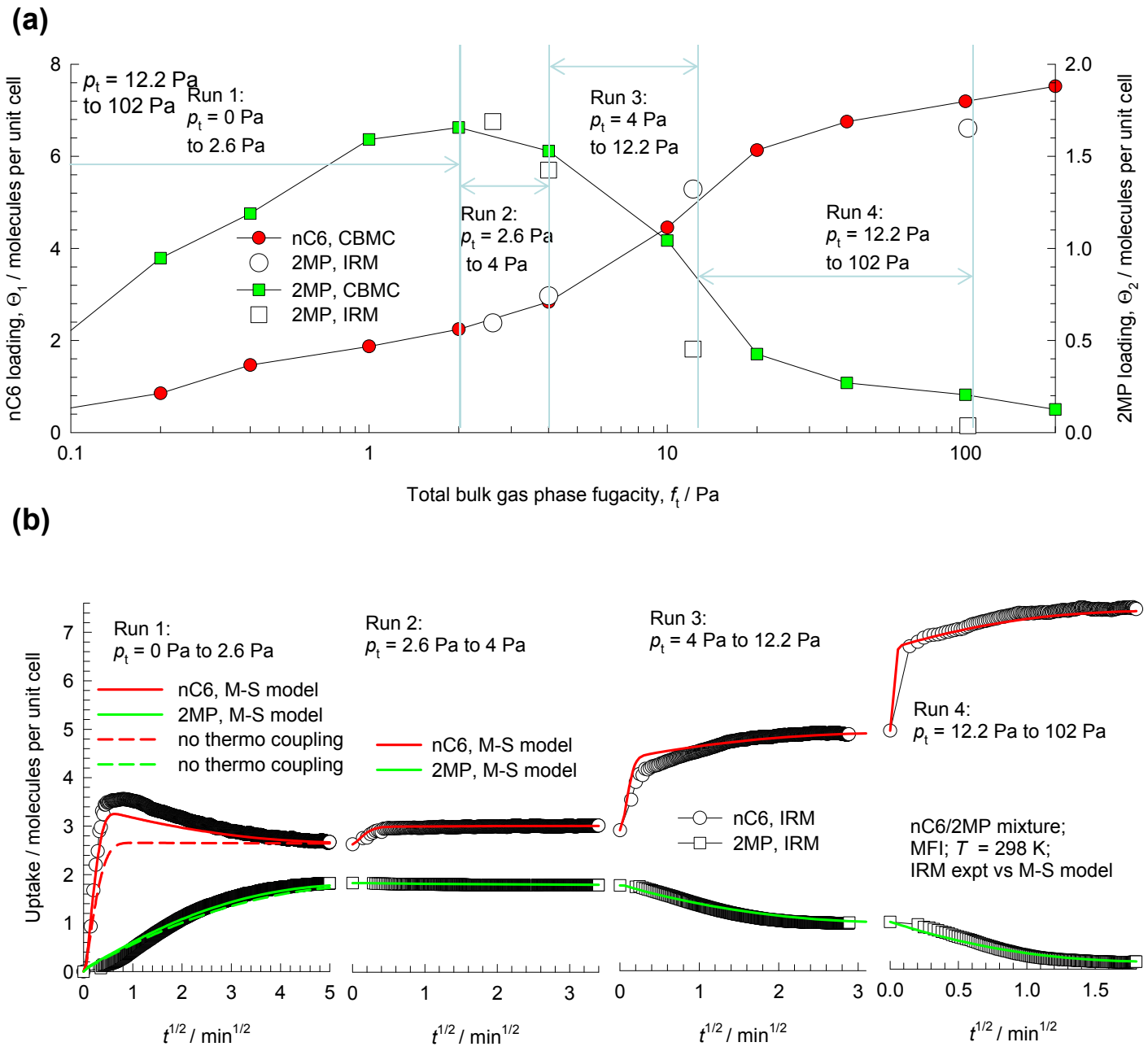
(a)
p_t = 12.2 Pa to 102 Pa
Run 1: p_t = 0 Pa to 2.6 Pa
Run 2: p_t = 2.6 Pa to 4 Pa
Run 3: p_t = 4 Pa to 12.2 Pa
Run 4: p_t = 12.2 Pa to 102 Pa
nC6, CBMC
2MP, IRM
2MP, CBMC
2MP, IRM
nC6 loading, Θ_1 / molecules per unit cell
2MP loading, Θ_2 / molecules per unit cell
Total bulk gas phase fugacity, f_t / Pa
(b)
Run 1: p_t = 0 Pa to 2.6 Pa
Run 2: p_t = 2.6 Pa to 4 Pa
Run 3: p_t = 4 Pa to 12.2 Pa
Run 4: p_t = 12.2 Pa to 102 Pa
nC6, M-S model
2MP, M-S model
no thermo coupling
no thermo coupling
nC6, IRM
2MP, IRM
nC6/2MP mixture;
MFI; T = 298 K;
IRM expt vs M-S model
Uptake / molecules per unit cell
$t^{1/2}$ / min$^{1/2}$

Figure 28

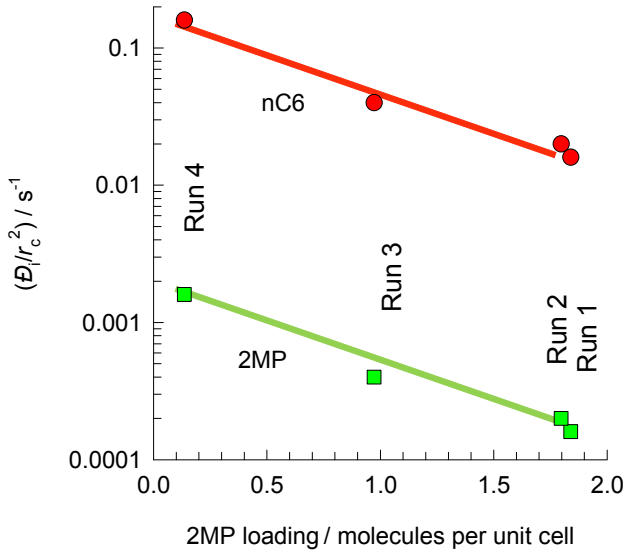
0.1
0.01
0.001
0.0001
0.0
0.5
1.0
1.5
2.0
nC6
2MP
Run 4
Run 3
Run 2
Run 1
$(Đ_i/r_c^2)$ / s^{-1}
2MP loading / molecules per unit cell

Figure 29

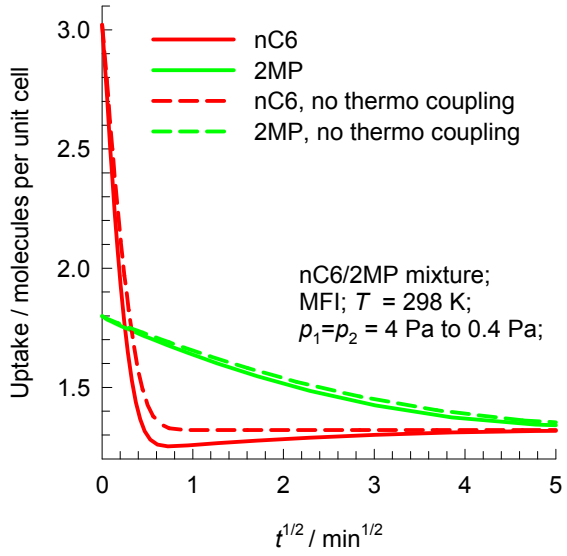
3.0
2.5
2.0
1.5
Uptake / molecules per unit cell
nC6
2MP
nC6, no thermo coupling
2MP, no thermo coupling
nC6/2MP mixture;
MFI; T = 298 K;
p1=p2 = 4 Pa to 0.4 Pa;
0
1
2
3
4
5
t1/2 / min1/2

Figure 30

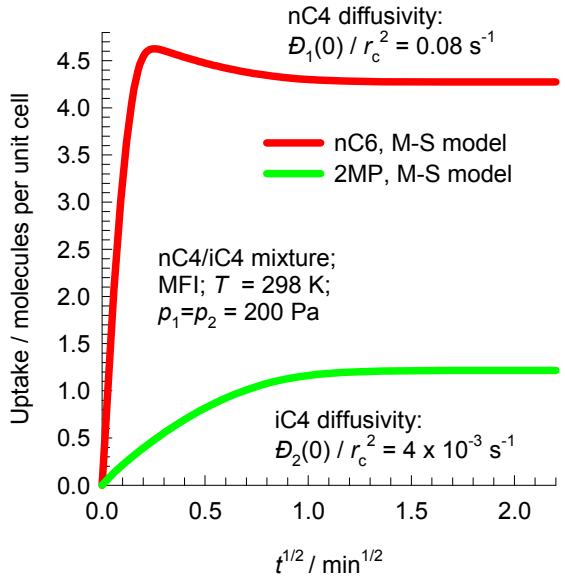
nC4 diffusivity:
$Đ_1(0) / r_c^2 = 0.08\ s^{-1}$
nC6, M-S model
2MP, M-S model
nC4/iC4 mixture;
MFI; T = 298 K;
$p_1 = p_2$ = 200 Pa
iC4 diffusivity:
$Đ_2(0) / r_c^2 = 4 \times 10^{-3}\ s^{-1}$
Uptake / molecules per unit cell
0.0
0.5
1.0
1.5
2.0
2.5
3.0
3.5
4.0
4.5
$t^{1/2}$ / $min^{1/2}$